

Astrocyte-oligodendrocyte interaction regulates central nervous system regeneration

Received: 18 October 2022

Accepted: 18 May 2023

Published online: 08 June 2023


 Check for updates

Irene Molina-Gonzalez ^{1,2,3,4}, Rebecca K. Holloway ^{1,2,3,4}, Zoeb Jiwaji ^{1,3}, Owen Dando ^{1,3}, Sarah A. Kent ^{1,2,3,5}, Katie Emelianova ^{1,3}, Amy F. Lloyd⁶, Lindsey H. Forbes ^{1,2,3,4}, Ayisha Mahmood ^{1,2,3,4}, Thomas Skripuletz⁷, Viktoria Gudi⁷, James A. Febery³, Jeffrey A. Johnson ^{8,9,10,11}, Jill H. Fowler³, Tanja Kuhlmann ¹², Anna Williams ^{1,2,13}, Siddharthan Chandran^{1,2,14}, Martin Stangel ⁷, Andrew J. M. Howden ⁶, Giles E. Hardingham^{1,2,3} & Veronique E. Miron ^{1,2,3,4,15,16,17} 

Failed regeneration of myelin around neuronal axons following central nervous system damage contributes to nerve dysfunction and clinical decline in various neurological conditions, for which there is an unmet therapeutic demand. Here, we show that interaction between glial cells – astrocytes and mature myelin-forming oligodendrocytes – is a determinant of remyelination. Using *in vivo*/ *ex vivo*/ *in vitro* rodent models, unbiased RNA sequencing, functional manipulation, and human brain lesion analyses, we discover that astrocytes support the survival of regenerating oligodendrocytes, via downregulation of the Nrf2 pathway associated with increased astrocytic cholesterol biosynthesis pathway activation. Remyelination fails following sustained astrocytic Nrf2 activation in focally-lesioned male mice yet is restored by either cholesterol biosynthesis/efflux stimulation, or Nrf2 inhibition using the existing therapeutic Luteolin. We identify that astrocyte-oligodendrocyte interaction regulates remyelination, and reveal a drug strategy for central nervous system regeneration centred on targeting this interaction.

Damage to myelin in the central nervous system (CNS) leads to loss of neuronal axon health and function in various neurological conditions (e.g. multiple sclerosis, spinal cord injury), which can be restored by the regeneration of myelin, termed remyelination¹. This involves the recruitment and differentiation of progenitor cells into mature oligodendrocytes, which must then survive to regenerate myelin². However, remyelination often fails with chronic myelin injury in association with continuous clinical decline. The unmet need for regenerative therapeutics highlights the importance of identifying which cellular interactions are critical for remyelination, and how these can be targeted to restore remyelination when it fails. Although current therapeutic strategies in development are focused on direct targeting of oligodendrocyte differentiation³, glial-glial interactions

are increasingly recognised as important regulators of myelin health^{4–8}. Astrocytes are promising therapeutic targets as they are the most abundant glial cell type in the CNS and communicate with oligodendrocytes in development to support initial myelin formation^{9,10}, yet their role in remyelination is understudied and controversial^{11–14}. To address this, we asked whether characterisation and manipulation of astrocytes during remyelination could reveal their regenerative function and a drug strategy to restore CNS regeneration. Here, we show that astrocytes have a role in supporting the survival of mature oligodendrocytes to ensure successful remyelination, and that this function is regulated by the downregulation of the Nrf2 pathway and concomitant upregulation of cholesterol biosynthesis/export.

A full list of affiliations appears at the end of the paper.  e-mail: veronique.miron@unityhealth.to

Results

Astrocytes become reactive during remyelination

We characterised astrocyte responses during efficient CNS remyelination *in vivo* by analysing focal lesions of myelin damage in the mouse corpus callosum, induced with the myelin toxin lyssolecithin (LPC). This model allows for the investigation of astrocytes during remyelination specifically, without concomitant damage, and has well-defined phases of completed myelin damage (demyelination, 3 days post-injection; DPI), oligodendrocyte differentiation and survival (7 DPI), early remyelination (10 DPI) and late remyelination (14–21 DPI)^{6,15,16} (Fig. 1a). During remyelination, densities of reactive astrocytes (GFAP+) and the proportion of total astrocytes (SOX9+) which were GFAP+ were increased compared to sham (PBS)-injected and no-lesion controls (Fig. 1b–d), confirmed by analysis of additional markers of astrocyte reactivity (Supplementary Fig. 1). Although total astrocyte numbers were slightly decreased early after myelin damage (3 DPI), these

recovered over the course of remyelination following proliferation (Supplementary Fig. 2). In an alternative model of demyelination induced by the oligodendrocyte toxin cuprizone in the diet, we observed similar changes in astrocyte responses during remyelination (Supplementary Fig. 3). These data demonstrate that astrocytes become reactive during remyelination.

Astrocytes downregulate the Nrf2 pathway and upregulate the cholesterol biosynthesis pathway during remyelination

To understand how these changes in astrocyte reactivity link to remyelination, we used translating ribosome affinity purification (TRAP) to isolate and sequence ribosome-associated mRNAs, which are being actively translated in astrocytes. To achieve this, we used a transgenic mouse in which the ribosomal subunit Rpl10a is tagged with eGFP driven by the pan-astrocyte-specific promoter for *Aldh1l1*¹⁷ (Fig. 1e); we confirmed that TRAP led to enrichment of mRNAs that

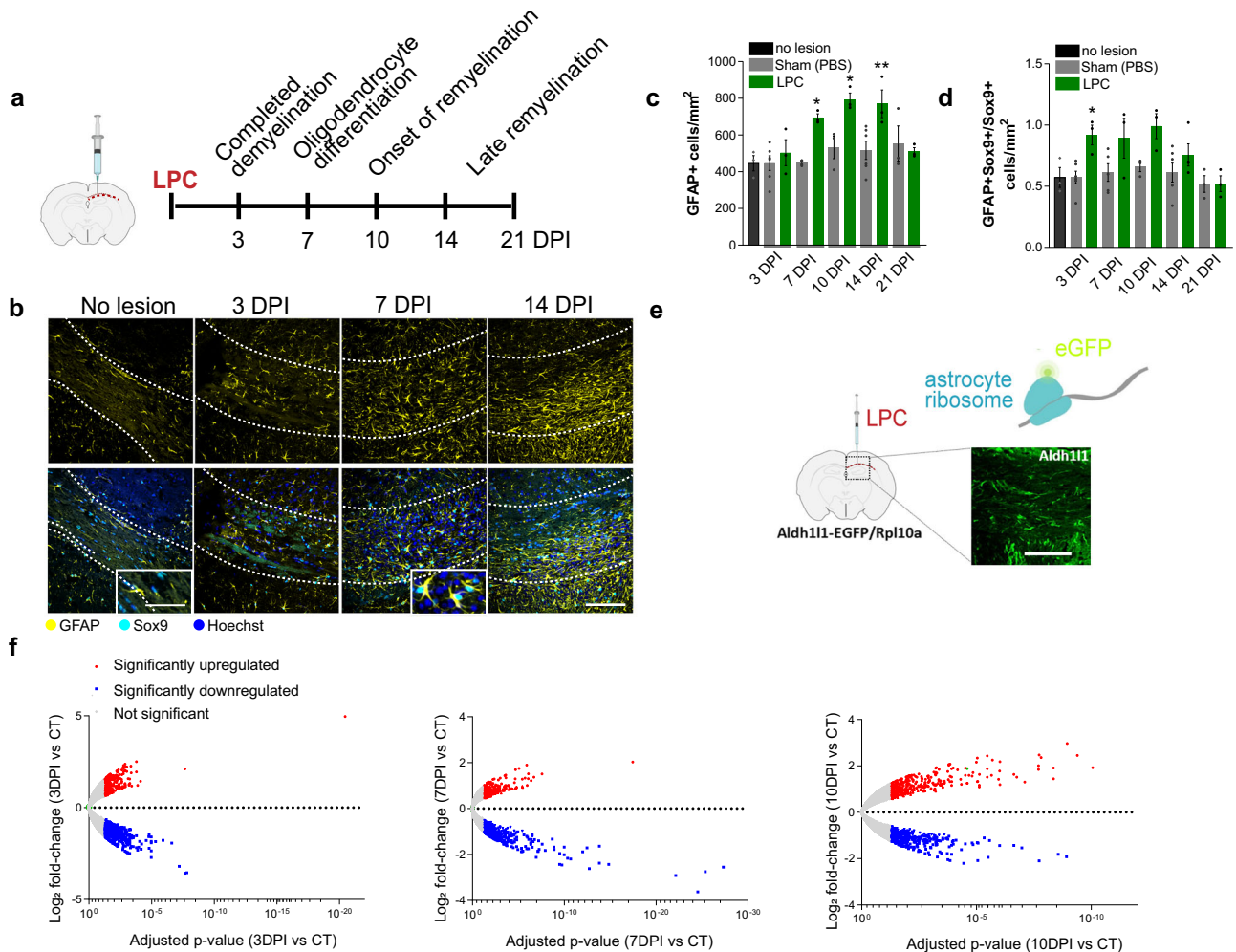


Fig. 1 | Astrocyte reactivity and translomes dynamically change during remyelination. **a** LPC-demyelinated lesions of adult mouse corpus callosum analysed at demyelination (3 DPI; days post-injection), oligodendrocyte differentiation/survival (7 DPI), the onset of remyelination (10 DPI) and late remyelination (14–21 DPI). **b** Reactive (GFAP+; yellow) astrocytes (SOX9+; cyan) in the corpus callosum (outlined) in no-lesion control and at 3, 7 and 14 DPI. Hoechst indicates nuclei in blue. Scale bar, 100 μ m. Inset: increased astrocyte hypertrophy over time. Scale bar, 50 μ m. **c** Mean GFAP+ cells/mm² \pm s.e.m. Two-way ANOVA with Sidak’s post hoc test versus sham, adjusted *P* values 0.0142 7 DPI, 0.0164 10 DPI and 0.0057 14 DPI. ANOVA summary (Interaction *P* = 0.0158, *F* = 3.338, Time *P* = 0.0011, *F* = 5.393, Condition *P* = 0.0002, *F* = 17.44). *n* = 3 mice/group (no lesion, 3, 7, 10, 14, 21 DPI LPC), *n* = 4 mice/group (7 DPI sham), *n* = 6 mice/group (3 and 14 DPI sham). **d** Mean proportion of GFAP + SOX9+ cells/mm² \pm s.e.m normalised to total SOX9+

cells. Two-way ANOVA with Sidak’s post hoc test versus sham, adjusted *P* value 0.0280 3 DPI. ANOVA summary (Interaction *P* = 0.2851, *F* = 1.322, Condition *P* = 0.0004, *F* = 16.35, Time *P* value = 0.0331, *F* = 3.036). *n* = 3 mice/group (no lesion, 3, 7, 10, 21 DPI LPC), *n* = 4 mice/group (14 DPI LPC), *n* = 5 mice/group (7 DPI sham), *n* = 6 mice/group (3 and 14 DPI sham). **e** TRAP of lesions in *Aldh1l1*-EGFP/Rpl10a mice by purification of eGFP-labelled ribosomes from astrocytes. Scale bar, 50 μ m. **f** Volcano plots of adjusted *P* values against Log₂ fold change at 3 DPI, 7 DPI and 10 DPI compared to control (CT), using a threshold of 1.3-fold and adjusted *P* value of <0.05. Red indicates upregulated genes, blue represents downregulated genes, and grey indicates genes which were not significantly changed. DESeq2 Benjamini–Hochberg test, adjusted *P* values <0.05. *n* = 3 mice/group. Source data is provided with this paper. The images in 1a and 1e were created with Biorender.com.

encode astrocyte-associated genes, and not those associated with other neural cells (Supplementary Fig. 4a). Compared to no-lesion control, there were significant changes in genes throughout remyelination, with 251 upregulated and 567 downregulated genes at 3 DPI, 236 upregulated and 387 downregulated genes at 7 DPI, and 398 upregulated and 413 downregulated genes at 10 DPI (≥ 1.3 -fold or ≤ -1.3 -fold change at adjusted p value < 0.05 ; Fig. 1f and Supplemental Data 1). The top 25 up- or downregulated genes were different at each time point, indicating changes in the translation of genes throughout remyelination (Supplementary Fig. 4b, c). Differentially expressed genes included those previously implicated in regulating remyelination, such as *Slpr3*, *Lgals1*, *Lgals3*, *Sema3a* (3 DPI), *Hmgcs2* (7 DPI), and *Lgals3* and *Cxcl5* (10 DPI). We investigated astrocyte phenotype by assessing expression of the top 50 genes previously shown to be induced in astrocytes in models of inflammation (induced by the bacterial peptide LPS) and neuroprotection (induced by cerebral artery occlusion)¹⁸ and found a mixed profile at all time points (Supplementary Fig. 5).

Our unbiased assessment of astrocyte phenotype identified engagement of the nuclear factor erythroid-2-related factor-2 (Nrf2) pathway at 3 DPI by Ingenuity Pathway Analysis (IPA; Nrf2-mediated oxidative stress response; Fig. 2a) and Gene Ontology (GO) term analysis (Wound healing involved in inflammatory responses; Supplementary Fig. 6a). This was of particular interest since Nrf2 has previously been shown to drive anti-oxidant and neuroprotective functions in astrocytes during myelin damage¹⁹. Classical Nrf2-target genes identified from pathway analysis (e.g. *Hmox1*) were transiently upregulated at 3 DPI versus no-lesion control (Fig. 2b), then subsequently downregulated at 7 DPI compared to 3 DPI (Fig. 2c). We confirmed the transient activation of the Nrf2 pathway at 3 DPI with increased activated Nrf2+ (nuclear expression) GFAP+ cells and HMOX1 + GFAP+ cells versus controls, which subsequently decreased by 7 DPI (Fig. 2d–g).

At 7 DPI, at the time of new oligodendrocyte generation and survival, we identified engagement of the cholesterol biosynthesis pathway by IPA (Superpathway of Cholesterol Biosynthesis, GGPP biosynthesis via mevalonate; Fig. 2h) and GO-term analysis (Cholesterol metabolism, Cholesterol homeostasis; Supplementary Fig. 6b). Cholesterol is known to support mature oligodendrocyte survival²⁰, and astrocytic cholesterol synthesis supports developmental myelination¹⁰ yet is dysregulated in neurological disease^{21,22}; however, the role of astrocytic cholesterol in remyelination specifically is unclear. We found that genes in the cholesterol biosynthesis pathway identified from pathway analysis were upregulated at 7 DPI versus no-lesion control (Fig. 2i). Genes in the cholesterol pathway were also upregulated at 7 DPI versus 3 DPI (Fig. 2j). This is in contrast to previously published astrocyte transcriptomes in the poorly remyelinating model experimental autoimmune encephalomyelitis (EAE), in which these genes are downregulated²¹. Astrocytes (GFAP+) positive for enzymes involved in cholesterol synthesis, HMGCS1 and FDPS, were significantly increased at 7 DPI versus controls (Fig. 2k–n), confirming engagement of this pathway.

We also observed these pathway changes in astrocytes in the cuprizone demyelination model. Densities of astrocytes with Nrf2 pathway activation were highest during the demyelination phase and early remyelination phase (3 and 5 weeks of cuprizone diet, respectively); during late-stage remyelination (7 and 10 weeks on a normal diet), Nrf2-activated astrocytes were decreased while astrocytes expressing cholesterol biosynthesis enzymes were increased (Supplementary Fig. 7). Our findings indicate that during remyelination, the Nrf2 pathway is de-activated in astrocytes coincident with activation of the cholesterol biosynthesis pathway. Interestingly, increased astrocytic cholesterol pathway activation occurred concomitantly with decreased activation of this pathway in the oligodendrocyte lineage at 7 DPI, suggesting potential compensation by astrocytes, whereas

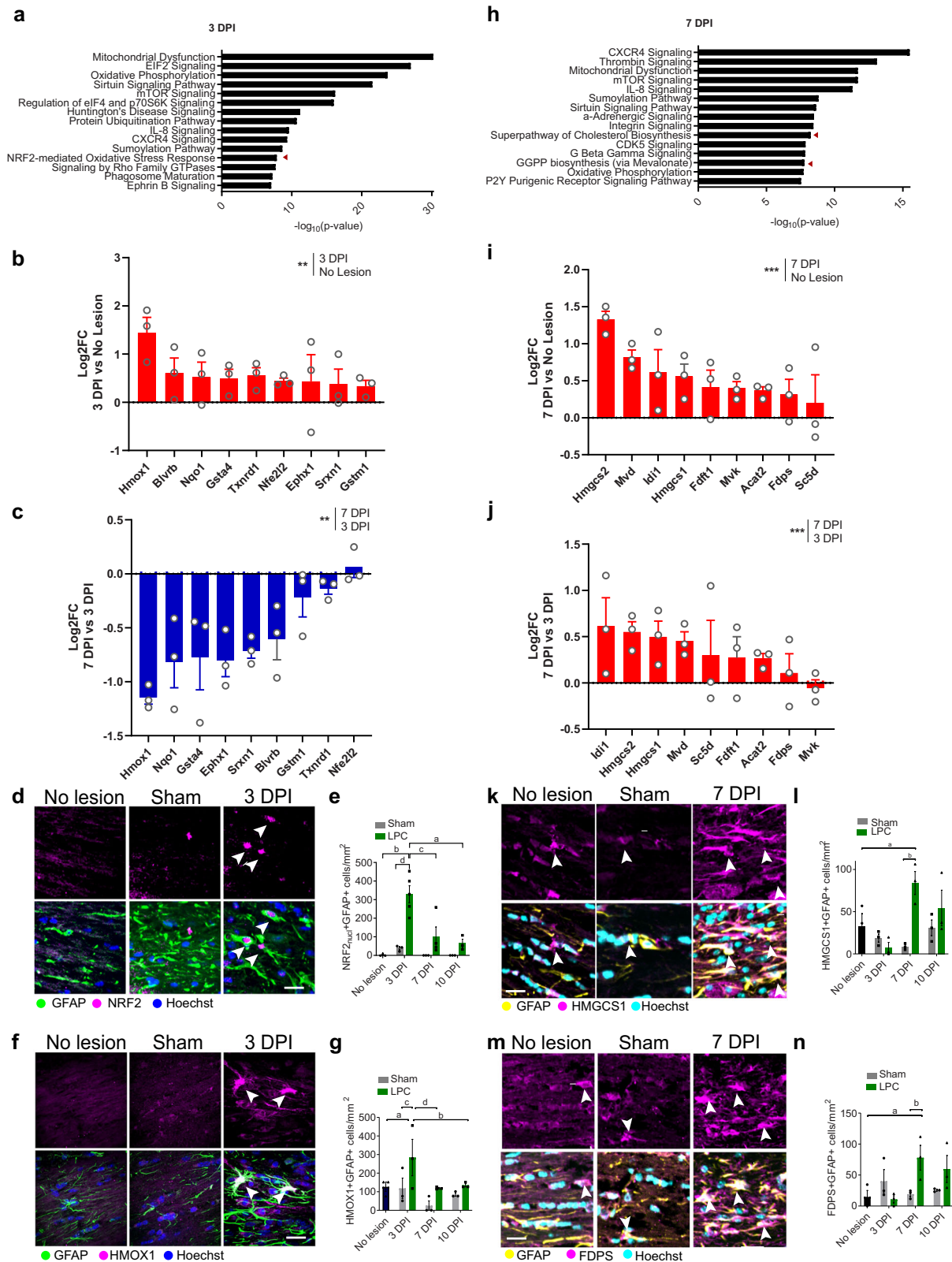
oligodendroglial Nrf2 activation was consistent throughout remyelination (Supplementary Fig. 8).

Manipulating astrocytic Nrf2 activation influences cholesterol pathway activation, oligodendrocyte survival and remyelination

Given that suppression of the Nrf2 pathway in the liver engages the cholesterol biosynthesis pathway^{23–26}, we postulated that the downregulation of the Nrf2 pathway in astrocytes permits subsequent activation of the cholesterol biosynthesis pathway during remyelination. To test this, we prevented Nrf2 pathway downregulation by using a transgenic mouse in which Nrf2 is constitutively overexpressed in reactive astrocytes (GFAP-Nrf2) (Fig. 3a), leading to persistent pathway activation^{27,28}. RNA sequencing of astrocytes in this model confirmed the upregulation of the Nrf2 gene (*Nfe2l2*) and Nrf2-target genes (Fig. 3b and Supplementary Fig. 9a), and staining of the tissue showed an increase in GFAP+ cells expressing the Nrf2 targets HMOX1 (Fig. 3c) and NQO1 (Supplementary Fig. 9b) in the corpus callosum compared to wildtype control. *Nfe2l2* upregulation was similar between astrocytes from GFAP-Nrf2 mice (fold change 2.3 versus wildtype control) and multiple sclerosis astrocytes (fold change 1.8 versus healthy control) (IPA Analysis Match^{19,29}), indicating a disease-relevant modulation of astrocytic Nrf2 activation in the mice. As neural stem cells (NSCs) can also express GFAP, we verified that the NSC marker MASH1 was not expressed by >99% of nuclear Nrf2+ cells in the corpus callosum of either wildtype or GFAP-Nrf2 mice (Supplementary Fig. 9c).

Early after demyelination, lesioned GFAP-Nrf2 mice showed decreased densities of reactive astrocytes (GFAP+; Fig. 3d, e) and total astrocytes (SOX9+; Supplementary Fig. 9d, e), which recovered by 14 DPI. We confirmed that reduced SOX9+ cells did not represent changes in oligodendrocytes, as the oligodendrocyte lineage marker SOX10 was not expressed by the majority of SOX9+ cells nor by >90% of GFAP+SOX9+ cells (Supplementary Fig. 9f–h). The reduction in astrocytes in GFAP-Nrf2 lesions may have been partially due to increased astrocyte apoptosis (active Caspase-3 + GFAP+; Supplementary Fig. 9i, j). We then assessed the impact of astrocytic Nrf2 activation on the cholesterol biosynthesis pathway, and found that the number of lesion GFAP+ cells that expressed cholesterol biosynthesis enzymes HMGCS1, FDPS, MVD and FDFT1 was significantly decreased in GFAP-Nrf2 mice compared to wildtype controls at 7 DPI, which remained low at 14 DPI (Fig. 3f–h and Supplementary Fig. 9k–m). The percentage of lesion astrocytes expressing HMGCS1 at 7 DPI was reduced from $40.2 \pm 4.6\%$ of GFAP+ cells in wildtype control to $7.5 \pm 5.0\%$ in GFAP-Nrf2 mice, which remained low by 14 DPI (Fig. 3i), indicating reduced engagement of the cholesterol biosynthesis pathway in surviving astrocytes in GFAP-Nrf2 mice. This was associated with an impairment in remyelination in GFAP-Nrf2 lesions at the time when it is normally robust (14 and 21 DPI), indicated by decreased expression of myelin proteins MBP (Fig. 3j, k) and CNPase (Supplementary Fig. 10a, b). Impaired remyelination in GFAP-Nrf2 mice was not the result of disrupted myelination at baseline as non-lesioned corpus callosum was unaffected (Fig. 3j, k), nor was demyelination more severe as the initial LPC-induced lesion was comparable to wildtype control (Supplementary Fig. 10c, d).

We did, however, observe decreased densities of total oligodendrocyte lineage cells (Olig2+; Fig. 3l) and oligodendrocytes (CC1+Olig2+; Fig. 3m) at 14 DPI in GFAP-Nrf2 mice, whereas these were unaffected in non-lesioned mice (Fig. 3l, m). The proportion of Olig2+ cells which were CC1+ or CC1- was not significantly affected in lesioned GFAP-Nrf2 mice (Fig. 3n), suggesting that oligodendrocyte differentiation was not impacted. To determine the cause of reduced oligodendrocyte lineage cells, we investigated their responses at earlier time points. No change was observed in the proportion of oligodendrocyte progenitor cells (OPCs; nuclear Olig1+) that were proliferating at 3 or 7 DPI (Ki67+; Supplementary Fig. 10e, f). However, GFAP-Nrf2 mice showed a significant increase in the proportion of



oligodendrocyte lineage cells undergoing cell death at 7 DPI (Olig2+ active Caspase-3+; Fig. 3o and Supplementary Fig. 10g), associated with a reduction in total Olig2+ cells (Supplementary Fig. 10h). These were found to be mature oligodendrocytes, as we observed a significant increase in the proportion of CCI1+ cells which were active Caspase-3+ (Supplementary Fig. 10i, j). These dysregulated oligodendrocyte responses in GFAP-Nrf2 lesions did not result from altered

microglial numbers nor their phagocytosis of myelin debris, which were not significantly changed compared to the control (Supplementary Fig. 10k, l). These findings associate sustained Nrf2 activation in astrocytes with reduced oligodendrocyte survival and poor remyelination.

As GFAP-Nrf2 lesions showed both a reduction in astrocyte numbers and impaired astrocytic cholesterol biosynthesis pathway

Fig. 2 | Astrocytes transiently engage the Nrf2 pathway followed by the cholesterol biosynthesis pathway during remyelination. **a** Top significantly engaged pathways at 3 days post-injection (DPI). Fisher's exact test, $P < 0.05$. **b** Log2 fold change (FC) of Nrf2-target genes at 3 DPI vs no-lesion control. $n = 3$ mice/condition. $^{**}P$ value = 0.0017, $t = 4.616$, two-tailed ratio paired t -test on expression (FPKM). **c** Log2FC of Nrf2 genes at 7 DPI vs 3 DPI. $n = 3$ mice/condition. $^{**}P$ value = 0.0068, $t = 3.621$, two-tailed ratio paired t -test on expression. **d** Nrf2+ (magenta) GFAP+ astrocytes (green) (arrows) at 3 DPI, Hoechst in blue. Scale bar, 25 μ m. **e** Nrf2 (nuclear)+ GFAP+ cells/mm² \pm s.e.m.. Two-way ANOVA with Tukey's multiple comparisons test, $^{a}P = 0.0002$, $^{b}P < 0.0001$, $^{c}P = 0.0004$, $^{d}P < 0.0001$. ANOVA summary (Interaction $F(4,12) = 5.897$, P value = 0.0024; Time-point factor $F(2,21) = 8.062$, P value = 0.0025; Condition factor $F(2,21) = 22.63$, P value < 0.0001). $n = 3$ mice/condition (no lesion, all sham, 10 DPI LPC), $n = 4$ mice/group (7 DPI LPC), $n = 5$ mice/group (3 DPI LPC). **f** HMOX1+ (magenta) GFAP+ astrocytes (green) (arrows) at 3 DPI. Hoechst in blue. Scale bar, 25 μ m. **g** HMOX1+ GFAP+ cells/mm² \pm s.e.m.. Two-way ANOVA with Tukey's multiple comparisons test, $^{a}P = 0.0377$, $^{b}P = 0.0292$, $^{c}P = 0.0280$, $^{d}P = 0.0166$. ANOVA summary (Interaction

$F(4,12) = 1.838$, P value = 0.1864; Time $F(2,12) = 4.66$, P value = 0.0318; Condition $F(2,6) = 3.08$, P value = 0.1202). $n = 3$ mice/condition. **h** Top significantly engaged pathways at 7 DPI. Fisher's exact test, $P < 0.05$. **i** Log2FC of cholesterol pathway genes at 7 DPI vs control. $n = 3$ mice/condition. $^{***}P$ value = 0.0009, $t = 5.098$, two-tailed ratio paired t -test on expression. **j** Log2FC of cholesterol pathway genes at 7 DPI vs 3 DPI. $n = 3$ mice/condition. $^{**}P$ value = 0.0003, $t = 6.164$, two-tailed ratio paired t -test on expression. **k** HMGCS1+ (magenta) GFAP+ astrocytes (yellow) (arrows). Hoechst in cyan. Scale bar, 25 μ m. **l** Mean HMGCS1+ GFAP+ cells/mm² \pm s.e.m.. Two-way ANOVA with Tukey's multiple comparisons test, $^{a}P = 0.0276$, $^{b}P = 0.0015$. ANOVA summary (Interaction $F(4,12) = 4.9575$, P value = 0.0134; Time $F(2,12) = 3.75$, P value = 0.0543; Condition $F(2,6) = 2.546$, P value = 0.1582). $n = 3$ mice/condition. **m** FDPS+ (magenta) GFAP+ astrocytes (yellow) (arrows). Hoechst in cyan. Scale bar, 25 μ m. **n** Mean FDPS+ GFAP+ cells/mm² \pm s.e.m.. Two-way ANOVA with Tukey's multiple comparisons test, $^{a}P = 0.0094$, $^{b}P = 0.0155$. ANOVA summary (Interaction $F(4,12) = 1.838$, P value = 0.1864; Time $F(2,12) = 4.66$, P value = 0.0318; Condition factor $F(2,6) = 3.08$, P value = 0.1202). $n = 3$ mice/condition. Source data is provided with this paper.

activation, we next tested the contribution of both processes to oligodendrocyte death during remyelination. First, we asked whether inducing astrocyte death is sufficient to reduce oligodendrocyte survival. We induced astrocyte death during remyelination using transgenic mice in which GFAP-driven expression of thymidine-kinase renders astrocytes selectively vulnerable to apoptosis following ganciclovir administration, using the cuprizone model where this paradigm has been previously optimised¹². Astrocyte death was induced in early-phase remyelination (weeks 4–5 of cuprizone administration; Supplementary Fig. 11a–d), when the cholesterol pathway is not yet upregulated (Supplementary Fig. 7e–h). This was associated with a decrease in oligodendrocytes (CCI+) and an increase in apoptotic oligodendrocytes (active Caspase-3+ CCI+) (Supplementary Fig. 11b, e, f).

Second, we asked whether poor oligodendrocyte survival in GFAP-Nrf2 mice could be rescued by reinstating cholesterol biosynthesis pathway activation in astrocytes. We achieved this using a blood–brain-barrier (BBB)-permeable and molecularly specific agonist of the cholesterol transporter ABCA1 (CS-6253)³⁰, previously used to increase expression of cholesterol biosynthesis genes in astrocytes²¹ as they are the primary expressors of ABCA1 (www.brainrnaseq.org). We assessed ABCA1 expression during remyelination, first by proteomic analysis of wildtype lesions which indicated increased ABCA1 levels at 7 DPI alongside several cholesterol biosynthesis pathway proteins (Fig. 4a); our dataset was biased towards detecting astrocyte-associated proteins (Fig. 4b) whereas microglial proteins CD68, TMEM119, and P2RY12 were not detected likely due to sensitivity thresholds. We confirmed ABCA1 gene and protein expression were upregulated in astrocytes over the course of remyelination (Fig. 4c, d), with >80% of ABCA1+ cells being GFAP+ between 7 and 14 DPI (Fig. 4e). CS-6253 or vehicle control was administered to lesioned GFAP-Nrf2 mice at the time when the cholesterol biosynthesis pathway is activated in wildtype mice (7 DPI) until remyelination would normally be underway (14 DPI) (Fig. 4f). CS-6253 significantly increased the percentage of cholesterol biosynthesis enzymes in astrocytes (HMGCS1+ GFAP+) compared to vehicle control (Fig. 4g, h). CS-6253 did not significantly impact cholesterol biosynthesis enzyme expression by oligodendrocytes or microglia (Supplementary Fig. 12a–d), nor microglial lesion coverage (Supplementary Fig. 12e, f). Nonetheless, the possibility of off-target effects on other cell types must be taken into consideration. CS-6253 administration increased numbers of oligodendrocyte lineage cells (Olig2+; Fig. 4i, l) and oligodendrocytes (CCI+Olig2+; Fig. 4j–l), and significantly decreased apoptotic oligodendrocytes (active caspase-3+CCI+) in GFAP-Nrf2 mice compared to vehicle control (Fig. 4m). This led to a rescue in remyelination at 14 DPI (Fig. 4n, o). Altogether, these findings demonstrate that sustained Nrf2 activity in astrocytes compromises oligodendrocyte survival and

remyelination, and suggest that this could be partly due to an impairment in the astrocytic cholesterol biosynthesis pathway.

Having observed that sustained astrocytic Nrf2 activation inhibits cholesterol pathway activation, we next asked whether loss-of-function knockout of Nrf2 in astrocytes would have opposing effects. Due to the importance of astrocytic Nrf2 for neuronal health, we avoided potentially deleterious impacts of CNS-wide knockout by generating a localised knockout of *Nfe2l2* in astrocytes in the corpus callosum. *Nfe2l2*-floxed mice were stereotaxically injected with an AAV5 inducing GFAP promoter-driven Cre recombinase and GFP expression ('AAV-Cre'), as done previously^{31–33}, allowed to recombine over 5 days, before injecting LPC to induce a lesion. At 3 DPI in the AAV-Cre lesions, >89% of the GFP+ signal was GFAP+ and >98% of GFAP+ cells were GFP+ (Supplementary Fig. 13a–e). Nuclear Nrf2+GFAP+ cells were significantly decreased to 16%, compared to 63% in mice injected with a sham virus (AAV5-GFAP-eGFP; 'AAV Sham') (Supplementary Fig. 13f, g); this accelerated the Nrf2 downregulation in astrocytes to 3 DPI, up from 7 DPI when it naturally occurs (Supplementary Fig. 13h). Inducing this downregulation ahead of schedule by gene deletion resulted in an earlier upregulation of expression of cholesterol biosynthesis enzymes HMGCS1, FDPS, MVD, and FDFT1 in astrocytes at 3 DPI (Supplementary Fig. 13i, j, l–o), up from 7 DPI when it normally occurs (Supplementary Fig. 13k), confirming the impact of Nrf2 on this pathway. There were no significant impacts of Nrf2 conditional knockout on astrocyte number or demyelination (Supplementary Fig. 13p–r). This genetically-induced accelerated downregulation of Nrf2 caused a small but significant acceleration in the level of remyelination at 7 DPI, such that it was similar to the average MBP lesion coverage normally observed at 14 DPI in remyelinating wildtype lesions (Supplementary Fig. 13s, u). The small impact on remyelination likely reflects the low number of newly generated/ apoptotic oligodendrocytes which could be influenced by astrocytic responses this early in remyelination. By 14 DPI, remyelination in the AAV Sham control caught up with that in the AAV-Cre condition (Supplementary Fig. 13t, v), which was expected given that at this time in controls, we normally observe robust remyelination, associated with downregulation of astrocytic Nrf2 and upregulation of cholesterol pathway activation. Nonetheless, our findings indicate that shifting forward Nrf2 downregulation in astrocytes accelerates remyelination. Altogether, these findings indicate that Nrf2 regulation in astrocytes is sufficient to influence the cholesterol pathway and remyelination.

Astrocytes export cholesterol to oligodendrocytes in vitro to regulate their survival and remyelination

In development, newly generated oligodendrocytes are susceptible to cell death, yet cholesterol supports their survival^{10,20}. We, therefore, asked whether astrocytes support oligodendrocyte survival by directly

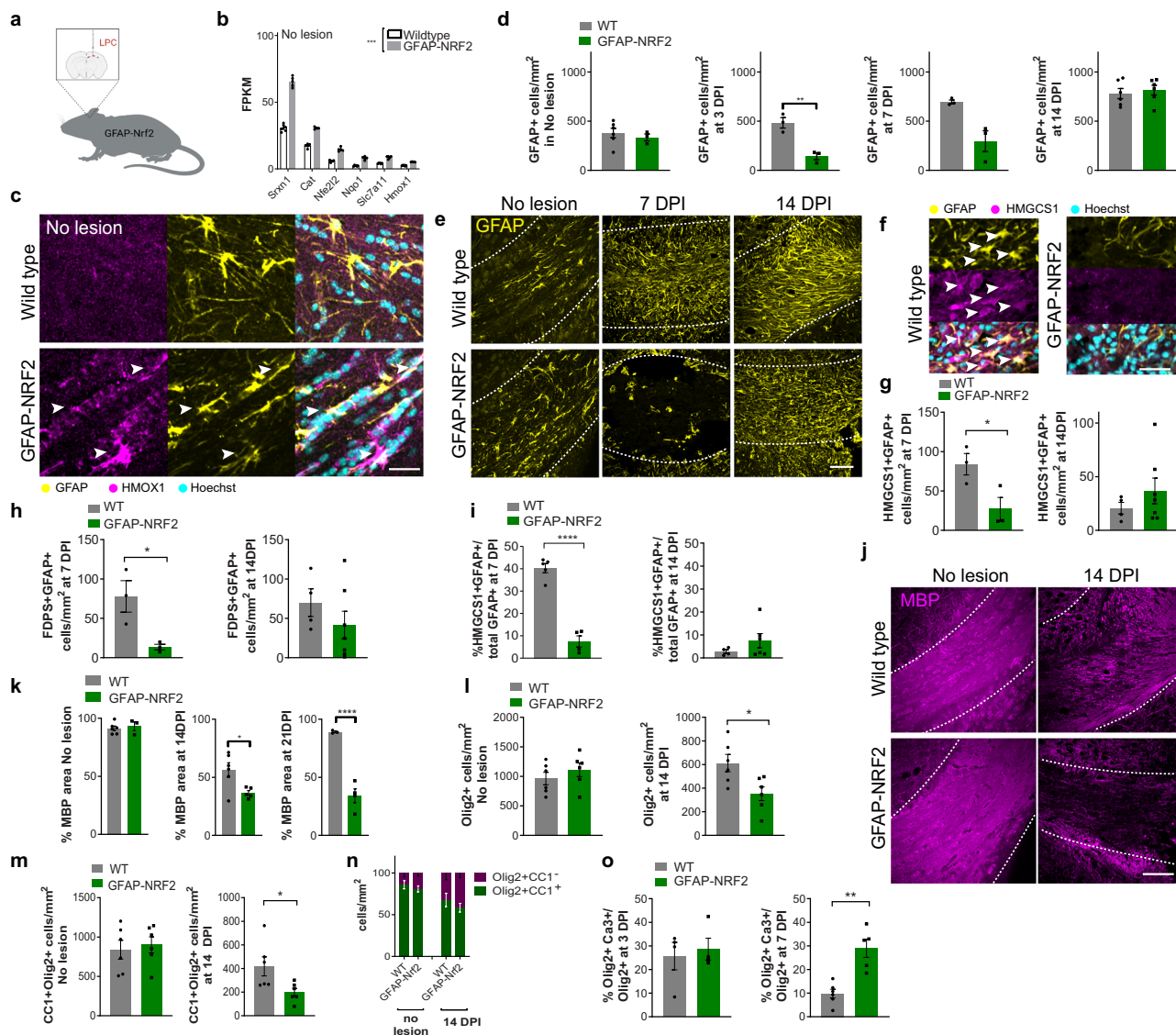


Fig. 3 | Astrocytic Nrf2 activation regulates oligodendrocyte survival and remyelination. a GFAP-Nrf2 maintain Nrf2 pathway activation in astrocytes. **b** Mean FPKM values \pm s.e.m. of Nrf2-target genes. two-tailed ratio paired *t*-test between wildtype and GFAP-Nrf2 mice in no-lesion conditions, P value = 0.0003, $t = 8.809$. $n = 6$ mice/condition (WT), $n = 5$ mice/condition (GFAP-Nrf2). **c** HMOX1+ (magenta) astrocytes (GFAP+) (arrows) in the non-lesioned corpus callosum. Hoechst in cyan. Scale bar, 25 μ m. **d** Mean GFAP+ cells/mm² \pm s.e.m. Two-tailed Mann-Whitney test, wildtype (WT) vs GFAP-Nrf2 in no lesion $P = 0.3810$, two-tailed unpaired Student's *t*-test with Welch's correction, WT vs GFAP-Nrf2, 3 DPI $P = 0.0089$ $t = 53.371$, 7 DPI $P = 0.0591$ $t = 3.711$, 10 DPI $P = 0.5754$ $t = 0.5791$. $n = 3$ mice/group (GFAP-Nrf2 no lesion, Wildtype and GFAP-Nrf2 3 and 7 DPI LPC), $n = 6$ mice/group (Wildtype no lesion, Wildtype and GFAP-Nrf2 14 DPI). **e** GFAP+ astrocytes (yellow) in the lesioned corpus callosum (outlined). Scale bar, 100 μ m. **f** HMGCS1+ (magenta) GFAP+ astrocytes (yellow)(arrows) in lesioned corpus callosum. Hoechst in cyan. Scale bar, 50 μ m. **g** Mean HMGCS1+GFAP+ cells/mm² \pm s.e.m.. Two-tailed unpaired Student's *t*-test with Welch's correction WT vs GFAP-Nrf2, 7 DPI $P = 0.0482$ $t = 2.823$, 14 DPI $P = 0.3112$ $t = 1.1$. $n = 3$ mice/condition (7 DPI), $n = 4$ mice/condition (14 DPI wildtype), $n = 7$ mice/condition (14 DPI GFAP-Nrf2). **h** Mean FDP5+GFAP+ cells/mm² \pm s.e.m. Two-tailed unpaired Student's *t*-test with Welch's correction WT vs GFAP-Nrf2, 7 DPI $P = 0.0398$ $t = 3.179$, 14 DPI $P = 0.2842$ $t = 1.148$. $n = 3$ mice/condition (7 DPI), $n = 4$ mice/condition (wildtype 14 DPI), $n = 7$ mice/condition (GFAP-Nrf2 14 DPI). **i** Mean percentage of GFAP+ cells positive for HMGCS1 \pm s.e.m. Two-tailed unpaired Student's *t*-test with Welch's correction WT vs GFAP-Nrf2, 7 DPI $P < 0.0001$ $t = 10.11$, 14 DPI $P = 0.1952$ $t = 1.469$. $n = 5$ mice/condition (wildtype 7 DPI), $n = 4$ mice/condition (GFAP-Nrf2 7 DPI),

wildtype 14 DPI), $n = 6$ mice/condition (GFAP-Nrf2 14 DPI). **j** MBP (magenta) in the corpus callosum (outlined). Scale bar; 100 μ m. **k** Percentage MBP area \pm s.e.m. Two-tailed unpaired Student's *t*-test with Welch's correction WT vs GFAP-Nrf2, no lesion $P = 0.6985$ $t = 0.4244$, 14 DPI $P = 0.0225$ $t = 3.047$, 21 DPI $P = 0.0024$ $t = 9.212$. $n = 3$ mice/condition (GFAP-Nrf2 no lesion, Wildtype 21 DPI LPC), $n = 4$ mice/condition (GFAP-Nrf2 21 DPI LPC), $n = 5$ mice/condition (GFAP-Nrf2 14 DPI LPC) $n = 6$ mice/condition (Wildtype no lesion, 14 DPI LPC). **l** Mean Olig2+ cells/mm² \pm s.e.m. Two-tailed unpaired Student's *t*-test with Welch's correction WT vs GFAP-Nrf2, no lesion $P = 0.3603$ $t = 0.9591$, 14 DPI $P = 0.0204$ $t = 2.777$. $n = 6$ mice/condition. **m** Mean CC1+Olig2+ cells/mm² \pm s.e.m. Two-tailed unpaired Student's *t*-test with Welch's correction WT vs GFAP-Nrf2, no lesion $P = 0.4435$ $t = 0.865$, 14 DPI $P = 0.0425$ $t = 2.508$. $n = 6$ mice/condition. **n** Proportion of Olig2+ cells that are CC1+ (green) or negative (magenta) \pm s.e.m. $n = 6$ mice/condition. Two-way ANOVA with Bonferroni correction, WT vs GFAP-Nrf2; no lesion, CC1+Olig2+ $P = 0.8323$ CC1-Olig2+ $P = 0.8322$, two-way ANOVA summary (Interaction $F(1,20) = 1.379$, P value = 0.2541; Genotype $F(1,20) = 3.171 \times 10^{-9}$, P value > 0.9999; Cell type $F(1,20) = 242.9$, P value < 0.0001). 14 DPI, CC1+Olig2+ $P = 0.6945$ CC1-Olig2+ $P = 0.6945$, ANOVA summary (Interaction $F(1,20) = 1.853$, P value = 0.1885; Genotype $F(1,20) = 0$, P value > 0.9999; Cell type $F(1,20) = 14.81$, P value = 0.0010). **o** Mean percentage of Olig2+ cells which are cleaved Caspase-3+ \pm s.e.m., at 3 DPI, two-tailed Mann-Whitney test, $P = 0.8857$; at 7 DPI, two-tailed unpaired Student's *t*-test with Welch's correction $P = 0.0044$, $t = 4.49$. $n = 4$ mice/condition (3 DPI), $n = 5$ mice/condition (GFAP-Nrf2 7 DPI), $n = 6$ mice/condition (wildtype 7 DPI). Source data is provided with this paper. The image in 3a was created with Biorender.com.

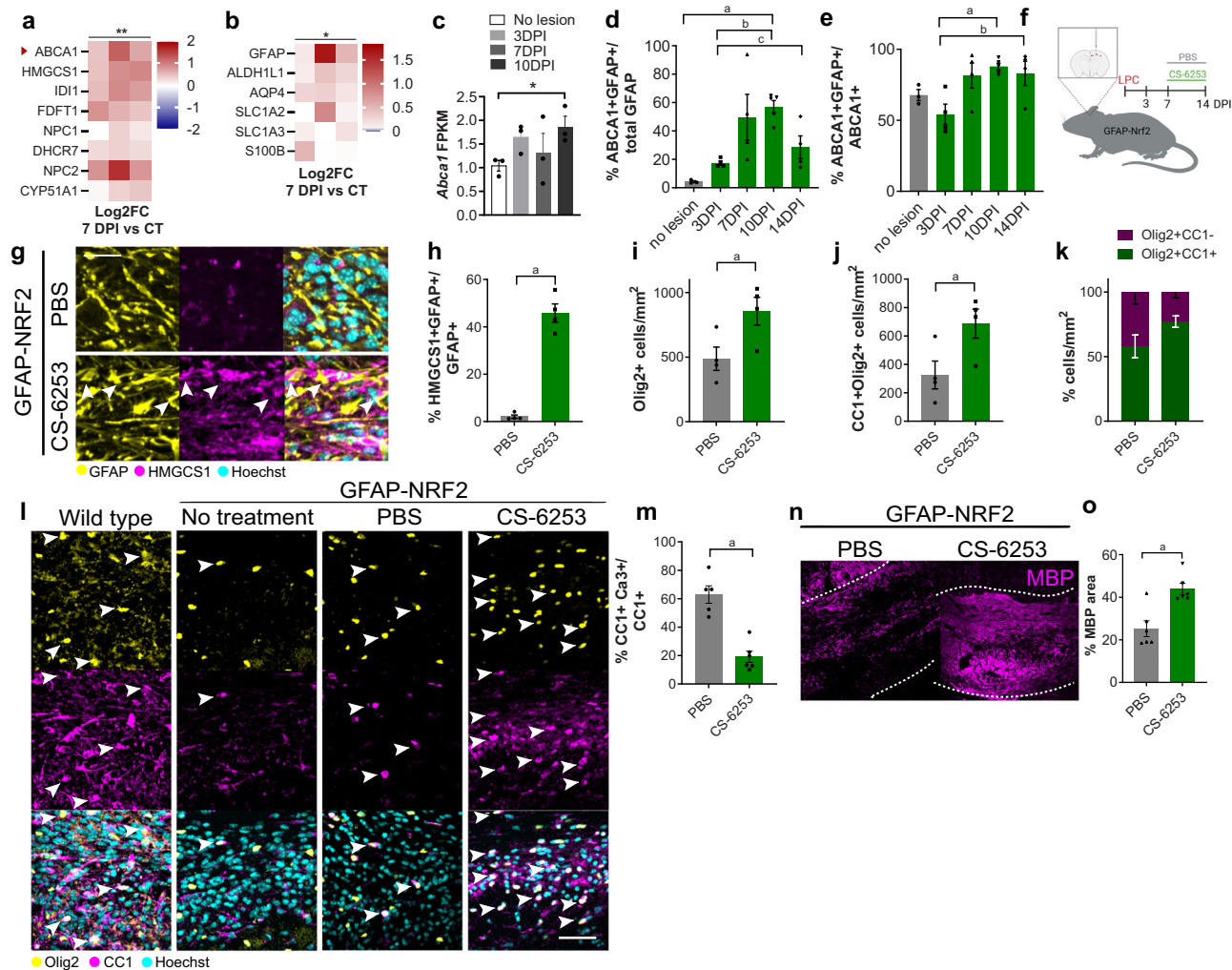


Fig. 4 | Stimulating the cholesterol biosynthesis pathway rescues oligodendrocyte survival and remyelination when astrocytic Nrf2 activation is sustained. **a** Proteomics of wildtype lesions at 7 DPI vs no lesion control (CT), represented as Log2FC of 7 DPI/CT. The two-tailed paired *t*-test between normalised intensities, *P* value = 0.0012, *t* = 5.228. *n* = 3 mice/condition. **b** Astrocyte-associated proteins in lesions at 7 DPI vs CT, represented as Log2FC. The two-tailed paired *t*-test between normalised intensities, *P* value = 0.0217, *t* = 3.291. *n* = 3 mice/condition. **c** Mean FPKM value \pm s.e.m. of *Abca1*. DESeq2 Benjamini–Hochberg test, adjusted *P* value $^aP = 0.042$. *n* = 3 mice/condition. **d** Percentage of GFAP+ cells expressing ABCA1 \pm s.e.m. One-way ANOVA with Tukey’s multiple comparisons test; $^aP = 0.0237$, $^bP = 0.0054$, $^cP = 0.0245$. ANOVA summary (*F* = 6.456 and *P* value = 0.0031). *n* = 3 mice/condition (no lesion), *n* = 4 mice/condition (3, 7, 14 DPI), *n* = 5 mice/condition (10 DPI). **e** Percentage of ABCA1+ cells expressing GFAP \pm s.e.m. One-way ANOVA with Tukey’s multiple comparisons test; $^aP = 0.0126$, $^bP = 0.0496$. ANOVA summary (*F* = 9.985 and *P* value = 0.0004). *n* = 3 mice/condition (no lesion), *n* = 4 mice/condition (3, 7, 14 DPI), *n* = 5 mice/condition (10 DPI). **f** CS-6253 or PBS was administered daily to LPC-lesioned GFAP-Nrf2 mice from 7–14 DPI. **g** HMGCs1+ (magenta) astrocytes (GFAP+; yellow) (arrows). Hoechst in cyan.

Scale bar, 25 μ m. **h** Percentage of GFAP+ cells expressing HMGCs1 \pm s.e.m., two-tailed Mann–Whitney test, $^aP = 0.0286$. *n* = 4 mice/condition. **i** Mean Olig2+ cells/mm² \pm s.e.m., two-tailed unpaired Student’s *t*-test with Welch’s correction, $^aP = 0.0413$, *t* = 2.61. *n* = 4 mice/condition. **j** Mean CC1+Olig2+ cells/mm² \pm s.e.m., two-tailed unpaired Student’s *t*-test with Welch’s correction, $^aP = 0.0432$, *t* = 2.555. *n* = 4 mice/condition. **k** Proportion of Olig2+ cells which were CC1+ (green) or CC1- (magenta) \pm s.e.m. Two-way ANOVA with Bonferroni correction PBS vs CS-6253, CC1+Olig2+ *P* value = 0.1597, CC1-Olig2+ *P* value = 0.1734. ANOVA summary (Interaction *F*(1,12) = 7.141, *P* value = 0.0203; Condition *F*(1,12) = 0.001127, *P* value = 0.9738; Cell type *F*(1,12) = 24.77, *P* value = 0.0003). *n* = 4 mice/group. **l** Oligodendrocyte lineage cells (Olig2+; yellow) which are mature (CC1+; magenta) (arrows). Hoechst in cyan. Scale bar, 50 μ m. **m** Percentage of CC1+ cells expressing active caspase-3 (Ca3+) \pm s.e.m., two-tailed unpaired Student’s *t*-test with Welch’s correction, $^aP = 0.0005$, *t* = 6.007. *n* = 5 mice/condition (PBS) and *n* = 6 mice/condition (CS-6253). **n** Myelin basic protein (MBP; magenta) in corpus callosum lesions (outlined). Scale bar, 100 μ m. **o** Percentage MBP area \pm s.e.m., two-tailed Mann–Whitney test, $^aP = 0.0260$, *n* = 6 mice/condition. Source data is provided with this paper. The image in 4f was created with Biorender.com.

exporting cholesterol to oligodendrocytes. As to our knowledge, technologies to assess cholesterol transfer between specific cell types in vivo are non-existent, precluding in vivo assessment. Therefore, as a proof-of-concept, we adopted a simplified in vitro model using primary cultures to directly manipulate isolated cell types. To assess the role of astrocytic Nrf2 activation in this process, we treated cultured primary astrocytes with the potent Nrf2 stimulator, the triterpenoid CDDO^{TFEA}^{34,35}, and subsequently with Luteolin—a flavonoid previously used to reduce Nrf2 hyperactivation³⁶, or CS-6253, to promote cholesterol synthesis and export (Fig. 5a). We confirmed increased

activated nuclear Nrf2 with CDDO^{TFEA} treatment which was abrogated using Luteolin, but not CS-6253, as expected (Fig. 5b, c). CDDO^{TFEA} upregulated Nrf2 pathway gene expression as expected, and downregulated expression of cholesterol pathway genes (Fig. 5d), demonstrating suppression of the cholesterol pathway by Nrf2 activation. Select cholesterol biosynthesis pathway gene expression was impacted in CDDO^{TFEA}-activated astrocytes with Luteolin or CS-6253 (Fig. 5e, f). Next, using a previously established in vitro method to track direct cholesterol transfer between cell types³⁷, we loaded astrocytes with the fluorescent cholesterol analogue Bodipy-FL-C12 for 6 h (Fig. 5a and

Supplementary Fig. 14), washing off excess, then allowing 18 h for analogue efflux into astrocyte-conditioned media (ACM), which was then applied to mature oligodendrocytes (Fig. 5g). Astrocyte cultures were confirmed to be pure via expression of marker *Aldh1l1* (Supplementary Fig. 14). Cholesterol analogue was taken up from ACM by mature oligodendrocytes (Bodipy+ TPPP/p25+), and an increased proportion of oligodendrocytes were Bodipy+ following treatment with ACM where astrocytic Nrf2 was inhibited (CDDO^{TEFA}/Luteolin ACM) or the cholesterol pathway was stimulated (CDDO^{TEFA}/CS-6253 ACM), compared to ACM generated from CDDO^{TEFA}-treatment alone (Fig. 5h, i). Immature oligodendrocyte lineage cells (Sox10+ TPPP/p25⁻) were not Bodipy+ (Fig. 5j). We next assessed the effect of ACM on oligodendrocyte survival. Oligodendrocytes matured in culture show a high level of baseline apoptosis (TUNEL+TPPP/p25+) ('OL media'). CDDO^{TEFA} ACM increased the percentage of apoptotic oligodendrocytes even further, whereas this was comparatively reduced with CDDO^{TEFA}/Luteolin or CDDO^{TEFA}/CS-6253 ACM (Fig. 5k, l). These results demonstrate a correlation between cholesterol analogue uptake from ACM and oligodendrocyte survival in vitro. To assess the relevance of remyelination, we applied ACM to brain explants after LPC-induced demyelination is complete (2 days post-LPC; dpl) until initiation of remyelination (5 dpl) (Fig. 5m). Whereas control explants exposed to unconditioned astrocyte media had little remyelination at this time, this was enhanced by exposure to untreated ACM as measured by remyelination index (MBP and NF colocalization normalised to NF; Fig. 5n, o). Conversely, exposure of brain explants to CDDO^{TEFA} ACM worsened remyelination, which was rescued by CDDO^{TEFA}/Luteolin or CDDO^{TEFA}/CS-6253 ACM (Fig. 5n, o). Although we recognise the limitations of in vitro experiments, this provided a proof-of-concept that, in principle, astrocytes export cholesterol to oligodendrocytes, this process is regulated by Nrf2, and this influences oligodendrocyte survival and remyelination in vitro/ex vivo. Future work is required to address this important question in vivo with the advent of new technologies.

We next hypothesised that astrocyte cholesterol efflux is a regulator of remyelination, which we tested by inhibiting cholesterol efflux from astrocytes using the ABCA1 inhibitor PSC833. Due to the inability of PSC833 to cross the blood–brain barrier, and the requirement for long-term treatment post-demyelination which precluded intracerebral injection, we applied the inhibitor to brain explants following demyelination (2 dpl) until remyelination is normally underway (7 dpl; Fig. 5p). Remyelination was impaired following treatment with PSC833 (1, 5, 10 μ M) compared to vehicle control (Fig. 5q, r). Taken together, these data suggest that astrocytes could regulate oligodendrocyte survival and remyelination via cholesterol efflux, yet this is impaired by Nrf2 activation.

Astrocytic Nrf2 activation in chronic human CNS lesions is associated with decreased cholesterol pathway activation and oligodendrocyte death

As Nrf2 activation in astrocytes is known to undergo changes in the human demyelinating disease multiple sclerosis (MS)^{19,38,39}, we investigated whether this was associated with altered cholesterol biosynthesis pathway activation. We analysed published single nuclei sequencing data of distinct MS lesion types in which remyelination potential is high ('active') or poor ('inactive') compared to previously remyelinated lesions ('remyelinated') and controls who died of non-neurological causes²⁹. Astrocytes were identified using the markers *AQP4* and *GFAP*, extracted using Seurat, and re-clustered at a resolution of 0.3 with a threshold of <15% mitochondrial RNA. Eight astrocyte clusters were identified, which demonstrated differential prevalence in MS lesions vs control, and active vs inactive lesions (Supplementary Fig. 15a). In particular, clusters 1 and 2 were predominantly detected in inactive lesions (Supplementary Fig. 15b). Of these two, cluster 1 astrocytes had enrichment of Nrf2-associated genes compared to all

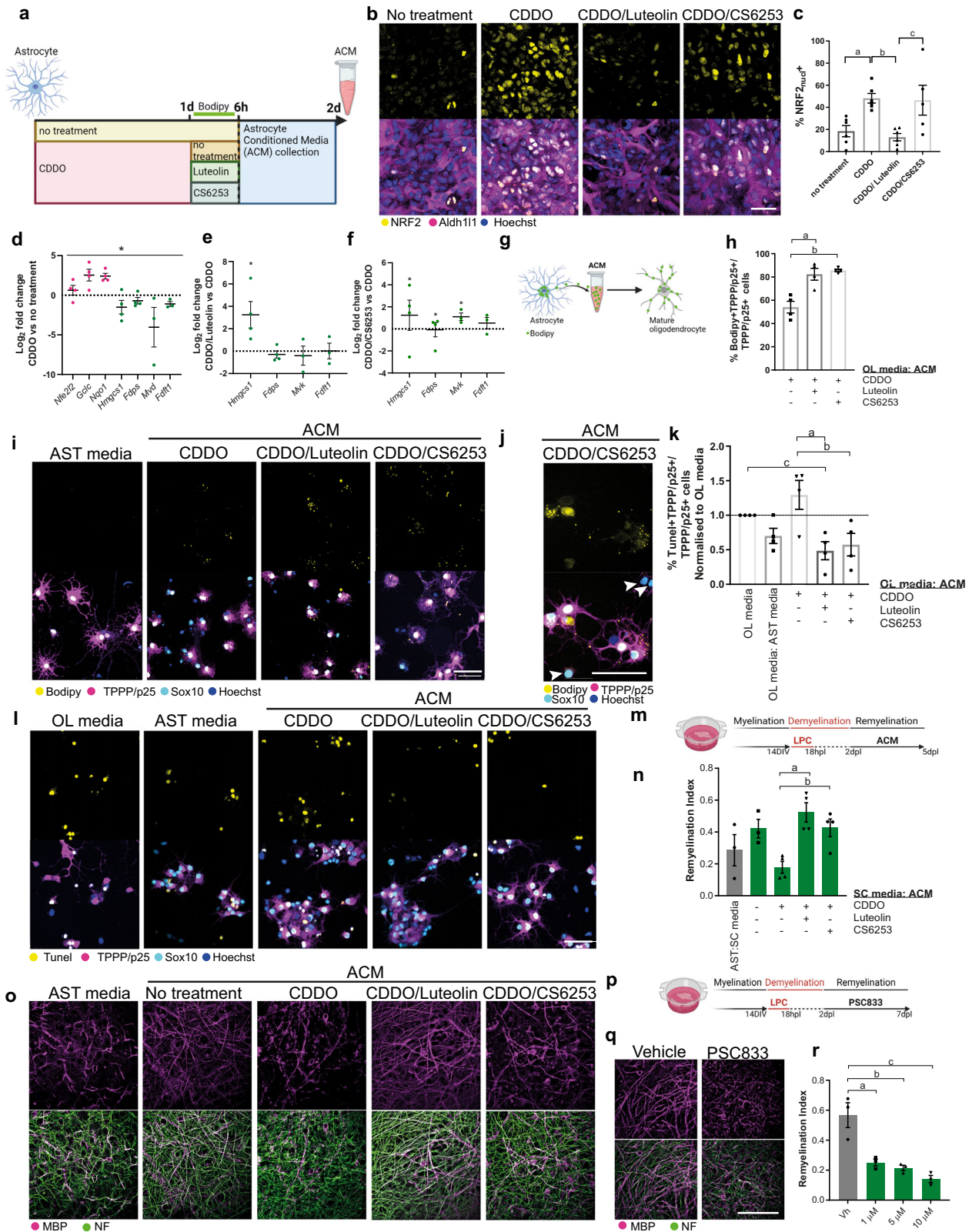
other clusters ($P = 0.0039$, Fisher's exact test and odds ratio 2.343). For instance, classical Nrf2-target genes *SLC7A11*, *MGST1* and *SQSTM1* have significantly increased expression in cluster 1 astrocytes compared to other clusters (Supplementary Fig. 15c). These same genes were also significantly increased in GFAP-Nrf2 astrocytes to a similar extent (Supplementary Fig. 15d). We found that cluster 1 astrocytes down-regulated cholesterol efflux genes (Supplementary Fig. 15e), thereby showing in human disease an association between Nrf2 engagement with cholesterol pathway downregulation in inactive MS lesion astrocytes. We validated these findings at the protein level (cases in Supplementary Table 1), finding that inactive lesions had the highest proportion of astrocytes positive for markers of Nrf2 activation (Nrf2, HMOX1, NQO1; Fig. 6a, b and Supplementary Fig. 15f–h) compared to active lesions, lesions that had already fully remyelinated, and controls. In contrast, these inactive lesions had a reduced proportion of astrocytes positive for the cholesterol biosynthesis pathway enzyme HMGCS1 compared to control and active or remyelinated lesions (Fig. 6c, d). Overall, these findings indicate activation of the Nrf2 pathway and suppression of the cholesterol biosynthesis pathway in inactive MS lesion astrocytes.

Given that our experimental findings suggest that sustained Nrf2 activation and poor cholesterol pathway activation in astrocytes leads to oligodendrocyte death in demyelinated lesions, we asked whether the association could also be made in MS lesions. Indeed, inactive lesions had reduced numbers of mature oligodendrocytes (TPPP/p25+Olig2+), and increased proportions of apoptotic (active Caspase-3+) Olig2+ or TPPP/p25+ cells (Fig. 6e–h). These findings are consistent with oligodendrocyte death recently being shown to contribute to poor remyelination in inactive MS lesions². Therefore, our results propose a link between dysregulated Nrf2 and cholesterol pathway activation in astrocytes with oligodendrocyte death and poor remyelination in humans.

Luteolin restores oligodendrocyte survival and remyelination efficiency

Given that sustained Nrf2 activation in astrocytes is associated with remyelination failure in mouse and human, we next sought to identify a drug candidate that could target this pathway to restore the efficiency of remyelination. We tested Luteolin, which is BBB-permeable, has an established safety profile in humans^{36,40} and potently decreases Nrf2 levels when it is over-activated (e.g. in tumours or in gain-of-function mutations^{36,41,42}), as observed in our in vitro assays (Fig. 5). Luteolin was administered to lesioned GFAP-Nrf2 mice when Nrf2 activation in wildtype astrocytes normally declines (4–7 DPI) (Fig. 7a); this decreased the proportion of GFAP+ cells with active nuclear Nrf2 in comparison to vehicle control (Fig. 7b, c). Luteolin restored astrocyte responses at 7 DPI, with a recovery in GFAP+ cells (Fig. 7d, e), a reduction in the proportion of GFAP+ active Caspase-3+ cells (Fig. 7d, f), and an increase in GFAP+ cells expressing the cholesterol biosynthesis enzyme HMGCS1 (Fig. 7g, h). Luteolin may have off-target effects on other cell types; although Luteolin also decreased Nrf2 activation in microglia, this did not significantly impact their expression of HMGCS1, their numbers, or their phagocytosis of myelin debris (Supplementary Fig. 16a–e). Direct treatment of primary microglia cultures did not impact their numbers or response to pro-inflammatory stimuli (Supplementary Fig. 16f).

We then asked how Luteolin-induced normalisation of astrocyte responses impacted the oligodendrocyte lineage and remyelination. Luteolin treatment of GFAP-Nrf2 mice restored numbers of oligodendrocyte lineage cells (Olig2+; Fig. 7i, j) and mature oligodendrocytes (CC1+Olig2+; Fig. 7i, k), increased the proportion of CC1+ cells (Fig. 7l), and decreased the proportion of Olig2+ cells which were active caspase-3+ (Fig. 7m, n). Importantly, Luteolin enhanced remyelination in GFAP-Nrf2 mice, with the percentage of MBP area significantly



increased over vehicle control (Fig. 7o, p). Luteolin had no impact on the number of oligodendrocyte lineage cells that express Nrf2 or HMGCS1 in the corpus callosum of GFAP-Nrf2 mice, nor did it affect oligodendrocyte lineage cell number or differentiation when delivered to purified primary cultures (Supplementary Fig. 16g–k). In addition, the beneficial response to Luteolin in vivo was limited to remyelination and not demyelination, as treatment of wildtype mice with Luteolin

during the time of LPC-mediated demyelination (0–3 DPI) had no impact on the percentage of MBP area or GFAP+ cells (Supplementary Fig. 16l–o). Luteolin may also act on other molecular targets; to address the specificity for Nrf2, we treated mice in which *Nfe2l2* was knocked out in astrocytes with Luteolin, and observed no additional effects on the cholesterol pathway or demyelination, nor was remyelination further increased (Supplementary Fig. 17), suggesting the

Fig. 5 | Astrocytes export cholesterol to oligodendrocytes to regulate their survival and remyelination. **a** Primary astrocytes treatment plan and collection of astrocyte-conditioned media (ACM). **b** Nrf2+ (yellow) astrocytes (Aldh1l1+; magenta), with Hoechst in blue, following treatment with CDDO^{TFEA} or CDDO^{TFEA}, then Luteolin, or CDDO^{TFEA} then CS-6253. Scale bar, 50 μ m. **c** Mean percentage of astrocytes expressing nuclear Nrf2 \pm s.e.m. One-way ANOVA and Tukey's multiple comparisons test; ^a $P=0.0286$, ^b $P=0.0085$, ^c $P=0.0178$. ANOVA summary $P=0.0023$, $F=6.994$. $n=6$ independent litters (no treatment, CDDO, CDDO/Luteolin, CDDO/CS-6253). **d** Astrocyte expression of genes involved in cholesterol and Nrf2 signalling following CDDO^{TFEA} treatment, represented as Log2FC over no treatment condition \pm s.e.m. One-tailed Wilcoxon test for $2^{-\Delta\Delta Ct}$, P value = 0.0156. $n=4$ independent litters (*Nfe2l2*, *Gclc*, *Nqo1*, *Hmgcs1*, *Fdps*) and $n=3$ independent litters (*Mvk*, *Fdft1*). **e** Astrocyte expression of genes after CDDO^{TFEA} treatment followed by Luteolin treatment, represented as Log2FC over CDDO^{TFEA} condition \pm s.e.m. Kolmogorov–Smirnov tests on $2^{-\Delta\Delta Ct}$, *Hmgcs1* $P=0.0286$. $n=4$ independent litters (*Hmgcs1*, *Fdps*) and $n=3$ independent litters (*Mvk*, *Fdft1*). **f** Astrocyte expression of genes after CDDO^{TFEA} treatment followed by CS-6253 treatment, represented as Log2FC over CDDO^{TFEA} condition \pm s.e.m. Kolmogorov–Smirnov tests on $2^{-\Delta\Delta Ct}$, *Hmgcs1* $P=0.0476$, *Fdps* $P=0.0476$, *Mvk* $P=0.0286$. $n=4$ independent litters (*Hmgcs1*, *Fdps*) and $n=3$ independent litters (*Mvk*, *Fdft1*). **g** ACM applied to oligodendrocytes to track the uptake of Bodipy-FL-C12 exported from astrocytes. **h** Percentage of TPPP/p25+ cells cholesterol which are Bodipy+ \pm s.e.m. Kruskal–Wallis test and Dunn's multiple comparisons test, ^a $P=0.0561$, ^b $P=0.0360$. $n=4$ independent litters. **i** Oligodendrocytes (TPPP/p25+ Sox10+; magenta/cyan) in unconditioned astrocyte media (AST) or following exposure to ACM, and uptake of Bodipy-FL-C12 (yellow). Hoechst in blue. Scale bar, 50 μ m. **j** Immature

oligodendrocyte lineage cells (Sox10+ TPPP/p25-) were Bodipy negative (arrows). Scale bar, 50 μ m. **k** Mean percentage of TPPP/p25+ cells which are Tunel+ \pm s.e.m., normalised to oligodendrocyte (OL) media control. Kruskal–Wallis test and Dunn's multiple comparisons test, P value = 0.0349, ^a $P=0.0083$, ^b $P=0.0265$, ^c $P=0.0265$. $n=4$ independent litters. **l** Apoptotic (Tunel+; yellow) TPPP/p25+ Sox10+ oligodendrocytes (magenta/cyan), in OL media or AST control, or following exposure to ACM. Scale bar, 50 μ m. **m** Brain explants myelinated for 14 days in vitro (DIV), were demyelinated with LPC, then fixed at 5 days post-LPC (dpl) when remyelination is initiated. **n** Remyelination index \pm s.e.m. for AST: slice culture media (SC) control, or following exposure to ACM. Two-tailed unpaired Student's t -test with Welch's correction, ^a $P=0.0048$, $t=4.842$; ^b $P=0.0125$, $t=3.723$. $n=3$ mice/condition (AST:SC media, SC media: ACM), $n=4$ mice/condition (CDDO, CDDO+Luteolin, CDDO+CS-6253), $n=3$ mice/condition (AST:SC media, ACM no treatment). **o** Explants exposed to AST or ACM from astrocytes following no treatment or exposure to CDDO^{TFEA}, CDDO^{TFEA} then Luteolin, and CDDO^{TFEA} then CS-6253 stained for myelin basic protein (MBP; magenta) and neurofilament (NF; green). Scale bar, 50 μ m. **p** Explants myelinated for 14 DIV, were demyelinated with LPC, then treated with the ABCA1 inhibitor PSC833 or vehicle control from 2 to 7 dpl when remyelination is underway. **q** Explants treated with vehicle control or PSC833 (5 μ M) and stained for MBP (magenta) and neurofilament (NF; green). Scale bar, 50 μ m. **r** Remyelination index \pm s.e.m. for vehicle or PSC833-treated brain explants. One-way ANOVA with Tukey's multiple comparisons test, ^a $P=0.0052$, ^b $P=0.0026$, ^c $P=0.0007$. ANOVA summary ($F=17.11$ and P value = 0.0008). $n=3$ mice/condition. Source data is provided with this paper. The images in 5a, g, m, p were created with Biorender.com.

beneficial impact of Luteolin on remyelination occurred primarily via Nrf2 modulation. In summary, we identified Luteolin as a candidate therapy to correct the dysregulated Nrf2 activation in astrocytes in the context of chronic myelin deficit, and to restore oligodendrocyte survival and remyelination efficiency.

Discussion

Our study identifies astrocyte-oligodendrocyte interaction as a key determinant of CNS myelin regeneration (Supplementary Fig. 18), complementing growing evidence for glial–glial interactions regulating myelin health^{4–8}. Our finding that astrocytes support the survival of mature remyelinating oligodendrocytes has important implications for the field. First, together with mature oligodendrocyte death recently considered to contribute to remyelination failure in chronic human disease², we highlight the importance of expanding the target of current regenerative drug development beyond immature cells of the oligodendrocyte lineage³. Second, our discovery that sustained activation of Nrf2 in astrocytes induces oligodendrocyte death and prevents remyelination counters the widely held concept that Nrf2 activation is often neuroprotective, yet is consistent with myelin pathology observed in humans harbouring gain-of-function Nrf2 gene mutations³⁶. This calls for further investigation into the impact of existing Nrf2-stimulating drugs on remyelination in progressive chronic disease. The protective function of astrocytic Nrf2 in reducing autoimmune-mediated myelin damage^{19,43,44} suggests distinct molecular requirements for astrocytes to support myelin health during active damage, versus during regeneration once the damage has already been inflicted. Third, our discovery that astrocyte cholesterol efflux regulates oligodendrocyte survival and hence remyelination highlights oligodendroglial cholesterol uptake as a potential regulator of white matter health. Consistent with this finding, cholesterol is known to support oligodendrocyte survival²⁰ and myelin production^{45–48} in development, and remyelination in adulthood^{48,49}. We propose that this occurs via astrocyte-mature oligodendrocyte interaction in late remyelination, building on recent work demonstrating that a microglial-derived cholesterol precursor influences OPC differentiation in early remyelination⁴⁹—when we showed astrocyte-derived cholesterol synthesis to be low. Importantly, the cholesterol biosynthesis pathway is dysregulated in the context of chronic

demyelination in mice^{48,49} and humans⁴⁸, yet is impacted both positively and negatively by drugs in MS clinical trials^{47,50}. We now propose that a strategy to restore the cholesterol biosynthesis pathway in chronic disease is to correct the sustained activation of Nrf2 in astrocytes using Luteolin, to re-establish healthy astrocyte-oligodendrocyte interaction and remyelination efficiency. The established safety profile of Luteolin in humans^{51–53} and its availability as a dietary supplement^{51,53} highlight it as a promising regenerative therapy, in addition to drugs in clinical trial which directly impact the oligodendrocyte lineage^{48,54–56}.

Our work suggesting the importance of astrocyte-oligodendrocyte interactions in remyelination complements earlier work implicating other cell types (e.g. microglia, regulatory T cells, pericytes) and pathways (e.g. muscarinic receptor and oestrogen receptor signalling) in regulating OPC differentiation into remyelinating oligodendrocytes^{6,8,16,55–58}. These findings, taken together with our study, point to the possibility of combining therapeutic approaches targeting oligodendrocyte generation and survival for maximal remyelination efficiency. We put forward that targeting astrocyte-oligodendrocyte interaction is a promising strategy to promote CNS remyelination in chronic disease.

Methods

Animals

The research carried out in this study complies with all ethical regulations. Experiments were performed under a United Kingdom Home Office project licence issued under the Animals (Scientific Procedures) Act 1968 to V.E.M. (Project Licence number PP8451532), through the Animal Welfare and Ethical Review Board, and all experiments approved by the Named Animal Care and Welfare Officers. Mice were housed in IVCs in groups of 5 in a 12:12 h light: dark cycle with unrestricted access to food and water, at room temperature (between 18–23 °C) at 40–60% humidity. C57Bl/6J wildtype mice, *Aldh1l1*-EGFP/Rpl10a mice (stock no.030248), C57Bl/6-*Nfe2l2*^{tm1.1Sred}/Sb1sJ (stock no. 025433) and B6.Cg-Tg(Gfap-TK)7.1Mvs/J (stock no.005698) were purchased from Jackson Laboratories. GFAP-Nrf2.2 mice were generated as previously described in ref. 27 and bred in-house with C57Bl/6 mice. Genotyping was performed from ear punches using Transnetyx services. Wildtype littermates from the same colony were used as controls. For in vitro studies, Sprague-Dawley wildtype rats of postnatal

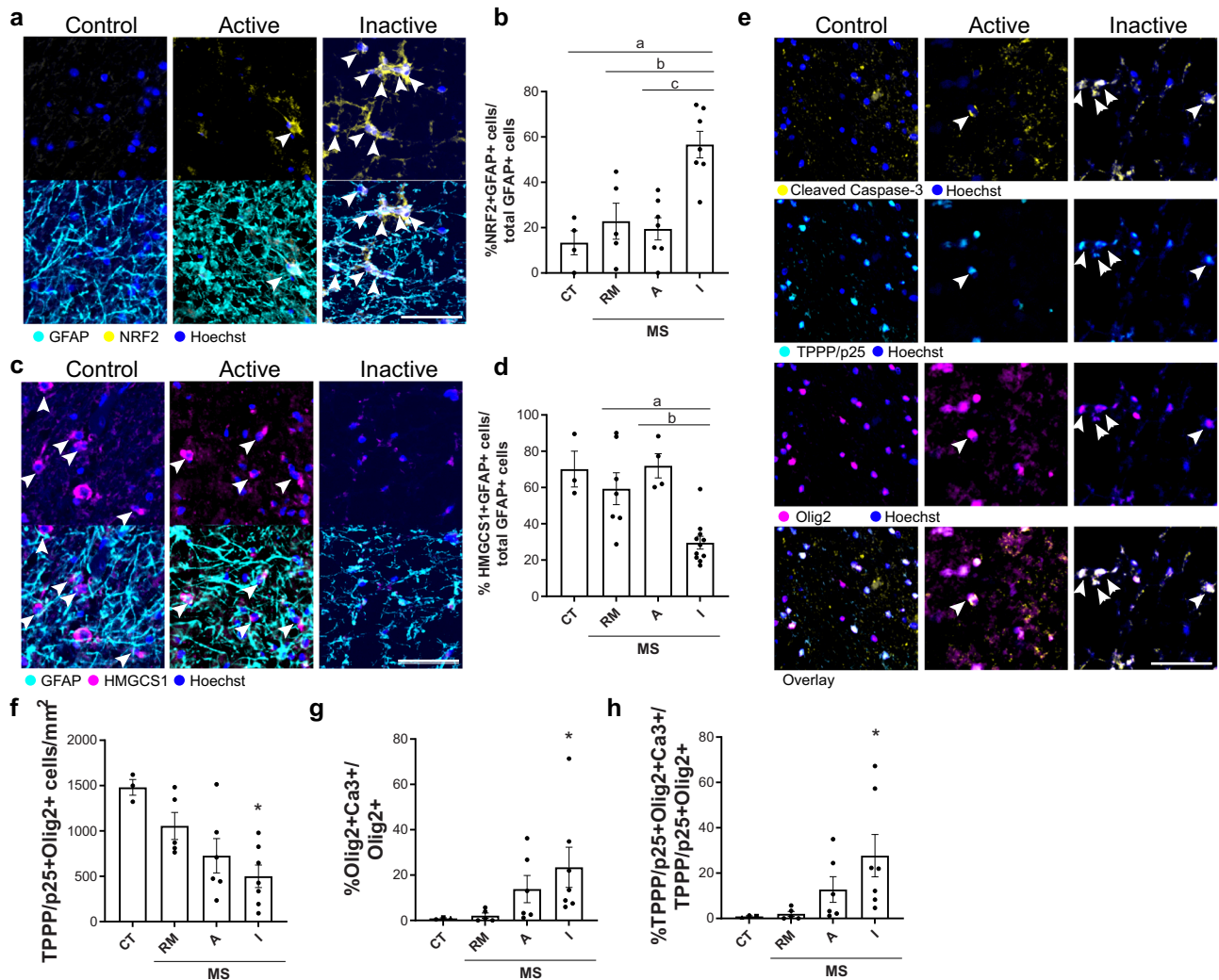


Fig. 6 | Astrocytic Nrf2 and cholesterol pathways are altered in chronic human brain lesions with poor remyelination potential and oligodendrocyte death.

a Nrf2⁺ (yellow) astrocytes (GFAP⁺; cyan) (arrows) with Hoechst in blue. Scale bar, 100 μ m. **b** Mean percentage of GFAP⁺ cells which are NRF2⁺ \pm s.e.m. in control (CT; $n = 4$), remyelinated (RM; $n = 5$), active (A; $n = 7$) and inactive lesions (I; $n = 7$) from multiple sclerosis (MS) cases. One-way ANOVA with Tukey's multiple comparisons test; ^a $P = 0.0008$, ^b $P = 0.0043$, ^c $P = 0.0007$. ANOVA summary ($F = 11.10$, P value = 0.0002). **c** HMGC1⁺ (magenta) astrocytes (GFAP⁺; cyan) (arrows) with Hoechst in blue. Scale bar, 100 μ m. **d** Mean percentage of GFAP⁺ cells which are HMGC1⁺ \pm s.e.m. in CT ($n = 3$), RM ($n = 7$), A ($n = 4$) and I lesions ($n = 11$) from MS cases. Kruskal–Wallis and Dunn's multiple comparisons test, ^a $P = 0.0429$, ^b $P = 0.0113$. KW summary (P value = 0.0009). **e** Active caspase-3⁺ (yellow) oligodendrocytes

(TPPP/p25⁺; cyan, and Olig2⁺; magenta) (arrows) with Hoechst in blue. Scale bar, 100 μ m. **f** Mean TPPP/p25⁺ Olig2⁺ cells/mm² \pm s.e.m. in CT ($n = 3$), remyelinated (RM; $n = 5$), active (A; $n = 6$) and inactive lesions (I; $n = 7$) from MS cases. Kruskal–Wallis with Dunn's multiple comparisons test, $P = 0.0284$ I vs CT. KW summary ($P = 0.0253$). **g** Mean percentage of Olig2⁺ cells expressing active caspase-3 (Ca3⁺)/mm² \pm s.e.m. in CT ($n = 3$), RM ($n = 5$), A ($n = 6$) and I lesions ($n = 7$) from MS cases. Kruskal–Wallis test and Dunn's multiple comparisons test, $P = 0.0251$ I vs R. KW summary ($P = 0.0090$). **h** Mean percentage of TPPP/p25⁺ Olig2⁺ cells expressing Ca3⁺/mm² \pm s.e.m. in CT ($n = 3$), RM ($n = 5$), A ($n = 6$) and I lesions ($n = 7$) from MS cases. Kruskal–Wallis with Dunn's multiple comparison test, $P = 0.0264$ I vs R. KW summary ($P = 0.0097$). Source data is provided with this paper.

days 0–3 (Charles River) were used. For ex vivo studies, CD-1 mice (Charles River) of postnatal days 0–3 were used. In vitro and ex vivo studies used rodents of both sexes.

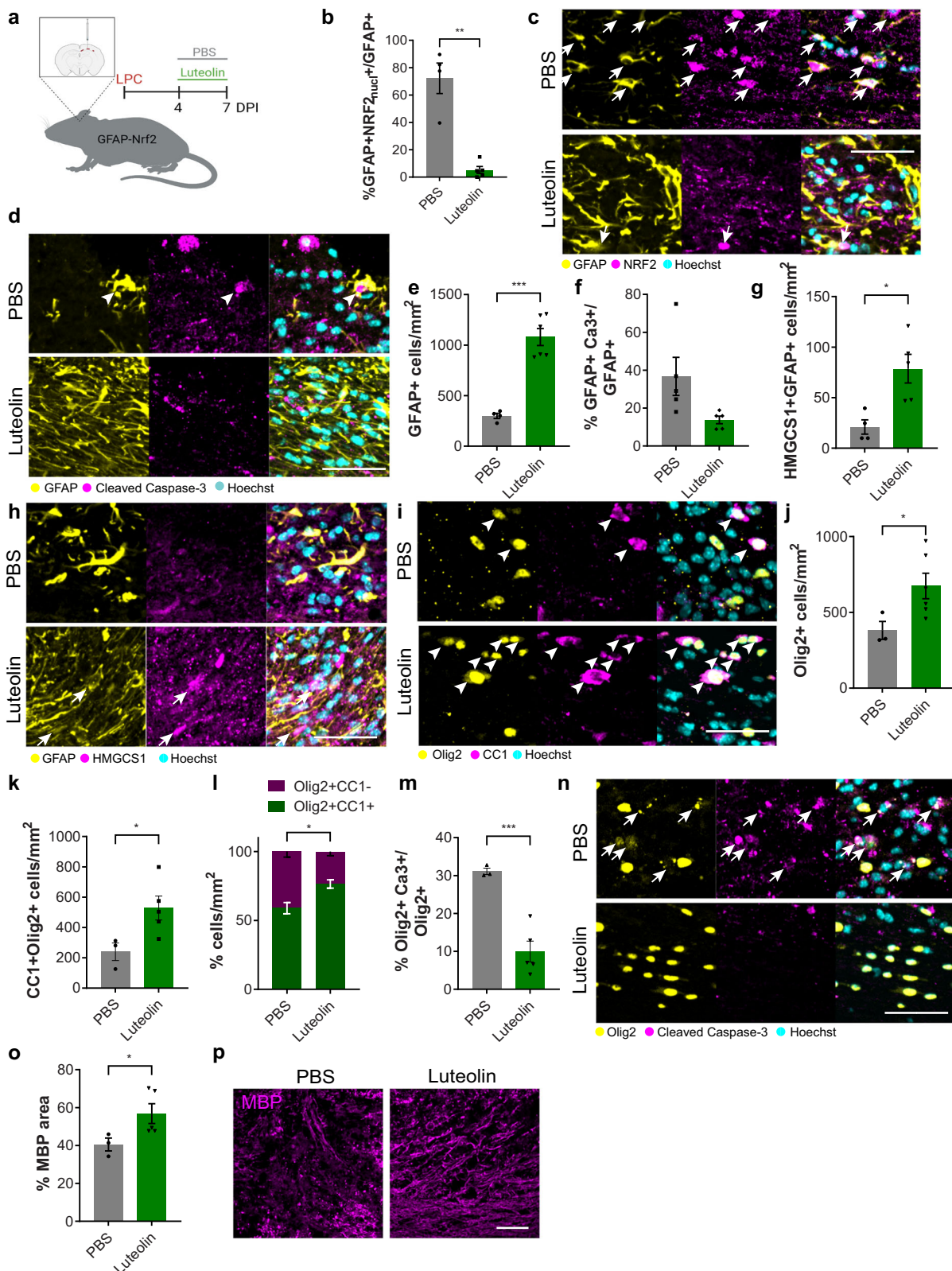
In vivo focal demyelination

About 2–3-month-old male mice were anaesthetised with isoflurane, administered analgesia (buprenorphine at 0.1 mg/kg and carprofen at 20 mg/kg, subcutaneous injection), then demyelinating lesions were induced by stereotaxically injecting 2 μ l of 2 μ g lysolecithin (LPC; egg yolk, Sigma-Aldrich Cat. No. L4129-100MG) diluted in phosphate-buffered saline (PBS) into the corpus callosum. Sham lesions were induced by injecting PBS. Mice were sacrificed for immunofluorescence analysis by intracardially perfused with 4% paraformaldehyde (PFA) at 3, 7, 10, 14 and 21 days post-injection (DPI), or by carbon dioxide (CO₂) asphyxiation at 3, 7, 10 DPI for translating

ribosome affinity purification (TRAP). For the former, brains were post-fixed overnight with 4% PFA, cryoprotected in sucrose and sectioned at 12- μ m thickness. The ABCA1 agonist CS-6253 (Biosynthesis Inc.)⁵⁹ was administered to demyelinated GFAP-Nrf2 mice from 7–14 DPI. CS-6253 was dissolved in PBS and injected intraperitoneally (i.p.) daily at 30 mg/kg as previously described in ref. 21. The Nrf2 inhibitor Luteolin⁴¹ was administered to demyelinated GFAP-Nrf2 mice from 4–7 DPI. Luteolin (Tocris Cat. No. 2874) was dissolved in 0.4 ml of PBS containing 1% dimethyl sulfoxide (DMSO, Sigma-Aldrich) to 500 μ M, which was administered daily by i.p. injection at 22.9 mg/kg.

In vivo cuprizone model of de- and remyelination

For assessment of astrocyte reactivity, numbers, proliferation, and expression of proteins in the Nrf2 and cholesterol biosynthesis pathways, male C57Bl/6 mice were fed with 0.3% cuprizone (Sigma-Aldrich)



mixed in powdered chow for 6 weeks, then fed with normal chow for weeks 7–10. Control mice were fed powdered chow without cuprizone. To ablate reactive astrocytes in the cuprizone model, GFAP-thymidine-kinase mice (Jackson Laboratories) were used in which thymidine-kinase from the herpes simplex virus is driven by the GFAP promoter. Mice were fed 0.2% cuprizone for 5 weeks, then returned to normal chow for 1 week. Either ganciclovir (200 mg/kg at first injection, then 25 mg/kg in

200 μ l of PBS) or PBS was administered to both control and transgenic mice from weeks 4–6 by daily i.p. injection. Mice were euthanised by intracardial perfusion-fixation under isoflurane, as above.

Conditional knockout of *Nfe2l2* in astrocytes

About 4–5-month-old male C57BL/6-*Nfe2l2*^{tm1.1Sred/SbisJ} mice were anaesthetised with isoflurane inhalation. 2.1×10^{10} genome copies of

Fig. 7 | Luteolin restores oligodendrocyte survival and remyelination when astrocytic Nrf2 is sustained. **a** Luteolin or PBS was administered to LPC-lesioned GFAP-Nrf2 mice from 4–7 DPI. **b** Mean percentage of GFAP+ cells with nuclear NRF2 (NRF2_{nuc}) ± s.e.m. Two-tailed unpaired Student's *t*-test with Welch's correction, $P = 0.0075$, $t = 5.851$. $n = 4$ mice/condition (PBS), $n = 5$ mice/condition (Luteolin). **c** Nrf2+ (magenta) astrocytes (GFAP+; yellow) (arrows) at 7 DPI. Hoechst in cyan. Scale bar, 50 μm . **d** Active caspase-3+ (magenta) astrocytes (GFAP+; yellow) (arrows) with Hoechst in cyan at 7 DPI. Scale bar, 50 μm . **e** Mean GFAP+ cells/mm² ± s.e.m. Two-tailed unpaired Student's *t*-test with Welch's correction, $P = 0.0001$, $t = 8.925$. $n = 4$ mice/condition (PBS), $n = 6$ mice/condition (Luteolin). **f** Percentage of GFAP+ cells positive for active caspase-3 (Ca3)/mm² ± s.e.m. Two-tailed unpaired Student's *t*-test with Welch's correction, $P = 0.0831$, $t = 2.245$. $n = 5$ mice/condition. **g** Mean HMGCS1+ GFAP+ cells/mm² ± s.e.m. Two-tailed unpaired Student's *t*-test with Welch's correction, $P = 0.0116$, $t = 3.642$. $n = 4$ mice/condition (PBS), $n = 5$ mice/condition (Luteolin). **h** HMGCS1+ (magenta) GFAP+ astrocytes (yellow)(arrows) at 7 DPI. Hoechst in cyan. Scale bar, 50 μm . **i** Oligodendrocyte lineage cells (Olig2+; yellow) which are mature (CC1+; magenta)(arrows) at 7 DPI. Hoechst in cyan. Scale bar, 50 μm . **j** Mean Olig2+ cells/mm² ± s.e.m., two-tailed

unpaired Student's *t*-test with Welch's correction, $P = 0.0253$, $t = 2.841$. $n = 3$ mice/condition (PBS) and $n = 6$ mice/condition (Luteolin). **k** Mean CC1+Olig2+ cells/mm² ± s.e.m., two-tailed unpaired Student's *t*-test with Welch's correction, $P = 0.0260$, $t = 2.938$. $n = 3$ mice/condition (PBS) and $n = 5$ mice/condition (Luteolin). **l** Proportion of Olig2+ cells which are CC1+ (green) or CC1- (magenta) ± s.e.m. Two-way ANOVA with Bonferroni correction, PBS vs Luteolin CC1+Olig2+ $P = 0.0088$, CC1-Olig2+ $P = 0.0086$. ANOVA summary (Interaction $F(1,14) = 23.04$, $P = 0.0003$; Condition $F(1,14) = 4.67 \times 10^{-5}$, P value = 0.9946; Cell type $F(1,14) = 93.77$, $P < 0.0001$). $n = 3$ mice/condition (PBS) and $n = 6$ mice/condition (Luteolin). **m** Mean percentage of Olig2+ cells which are active Ca3+ ± s.e.m., two-tailed unpaired Student's *t*-test with Welch's correction, $P = 0.0009$, $t = 7.326$. $n = 3$ mice/condition (PBS) and $n = 5$ mice/condition (Luteolin). **n** Active Caspase-3+ (magenta) oligodendrocyte lineage (Olig2+; yellow)(arrows). Hoechst in cyan. Scale bar, 50 μm . **o** Percentage MBP area ± s.e.m. Mann-Whitney test, $P = 0.0357$. $n = 3$ mice/condition (PBS) and $n = 5$ mice/condition (Luteolin). **p** MBP (magenta) at 7 DPI. Scale bar, 50 μm . Source data is provided with this paper. The image in 7a was created with Biorender.com.

AAV5-GFAP(0.7)-EGFP-T2A-iCre (Vector Labs, Cat. No. VB1131) or AAV5-GFAP(0.7)-EGFP (Vector Labs, Cat. No. VB1149) were stereotaxically injected into the corpus callosum at an infusion rate of 200 nl/ml. Recombination was allowed for 5 days before inducing demyelination with LPC, as above, and sacrificed 3, 7 or 14 days post-LPC. A subset of AAV5-GFAP(0.7)-eGFP-T2A-iCre-treated *Nfe2l2*-floxed mice were treated daily with Luteolin as above from the time of LPC injection to 3 or 7 days post-LPC. Mice were euthanised by intracardial perfusion-fixation under isoflurane, as above.

Immunofluorescence of in vivo tissue sections

Paraffin-embedded sections of brains from cuprizone-fed mice were pre-heated at 60 °C for 20 min, immersed in Histoclear II and progressively rehydrated in descending ethanol gradients (100, 95, 70, 50 %) and water. Frozen sections of brains from LPC-injected mice were air-dried for 15 min. Heat-induced antigen retrieval was achieved by microwaving sections at medium power in 10 mM citrate buffer (pH 6.0) and heating for 20 min at 60 °C, followed by PBS washes. Slices were blocked for 1 h (5% horse serum and 0.3% Triton X in PBS), then incubated with primary antibodies overnight at 4 °C in a humid chamber. Antigen retrieval for myelin proteins such as MBP and MAG was achieved by immersing the slides in cold methanol at -20 °C for 20 min, then washing with PBS. The following antibodies were used: rat anti-myelin basic protein (MBP, 1:100, Bio-Rad antibodies MCA409S), mouse anti-myelin-associated glycoprotein (MAG, 1:100, Sigma-Aldrich MAB1567), chicken anti-gial fibrillary acidic protein (GFAP, 1:500, Bio-Legend PCK-591P), chicken anti-GFAP (1:500, Cambridge Bioscience 829401), rabbit anti-SOX9 (1:500, Sigma-Aldrich AB5535), mouse anti-Nestin (1:100, Abcam ab6142), mouse anti-vimentin (1:100, Sigma-Aldrich clone LN-6 MAB1681), rabbit anti-nuclear factor IA (NFIA, 1:250, Abcam ab228897), rabbit anti-Ki67 (1:500, Sigma-Aldrich AB9260), mouse anti-APC (CC1, 1:100, Abcam ab16794), rabbit anti-Olig2 (1:100, Sigma-Aldrich AB9610), rabbit anti-HMOX1 (1:100, Enzo ADI-SPA-895-D), rabbit anti-HMGCS1 (1:500, Invitrogen PA5-29488), rabbit anti-FDPS (1:500, Invitrogen PA5-28228), anti-MVD antibody (1:100, Abcam ab198823) rabbit anti-FDFT1 (1:100, Abcam ab236666), rabbit anti-IBA1 (1:500, Abcam 178846), rabbit anti-ABCA1 (1:100, Novus Biologicals NB400-105), mouse anti-Sox10 (1:100, Sigma-Aldrich AMAB91297), mouse anti-Olig1 (1:1000, EMD Millipore MAB5540), rabbit anti-active Caspase-3 (1:500, BD Pharmingen 559565), mouse anti-CNPase (1:2000, Sigma-Aldrich AMAB91072), mouse anti-MASH1 (1:100, BD Bioscience 556604), rabbit anti-NQO1 (1:100, Abcam ab2346), rat anti-NRF2 (1:500, Cell Signalling 14596 S) and chicken anti-GFP (1:100, Abcam ab13970). Following washes with PBS, Alexa-conjugated secondary antibodies (all at 1:500, Life Technologies; A21202, A10042, A21235, A21449, A11039, A21206, A11055, A21434, A31573, A31570, A21247, A212469 and

A11006) and Hoechst (Sigma-Aldrich) were applied for 2 h at 20–25 °C in a humid chamber. Slides were coverslipped with Fluoromount-G (Cambridge Biosciences). Z-stacks of images were obtained using an Olympus 3i Spinning Disk confocal microscope (30x silicone objective) and SlideBook 6 software.

Magnetic cell separation (MACS), RNA extraction and bulk RNA sequencing

Brains were dissociated using a gentle MACS Dissociator, and astrocytes were isolated using the Anti-ACSA-2 MicroBead Kit (Miltenyi Biotec). RNA sequencing was performed using TrueSeq Stranded Total RNA V2 library preparation along with next-generation sequencing on the Illumina Novaseq 6000 platform with an approximate read-depth of 90 million reads per sample. At least 1 μg RNA per sample was utilised, with RNA integrity number (RIN) >7.

Translating ribosome affinity purification (TRAP), RNA extraction and RNA sequencing

Corpus callosa were dissected from LPC-injected and non-lesioned mice and were processed for TRAP as done previously¹⁷. RNA was extracted from pre-TRAP controls ('Input') and TRAP samples using the Agilent Nanoprep kit. The quality of the samples was measured using an Agilent Bioanalyzer and the Agilent RNA 6000 PICO assay protocol. Samples selected had an RNA integrity number (RIN) >7 and were sent to Cambridge Genomic Services for Next-Generation Sequencing. For library preparation, the SMART-Seq v4 Ultra Low Input RNA kit (Takara Bio USA) was used according to the manufacturer's instructions. The sequencing was run on a NextSeq 550 system (Illumina) on a 150-cycle high-output run with paired-end reads (30 million reads). For each TRAP sample, 75 base pair paired-end reads were mapped to the primary assembly of the mouse (mm10) reference genome contained in Ensembl release 93. Alignment was performed with STAR version 2.5.3a. Per-gene read counts were summarised using featureCounts version 1.5.2.

Differential expression and pathway analysis

Differential expression analysis was performed using DESeq2 (R package version 1.18.1), with a significance threshold calculated at a Benjamini-Hochberg-adjusted *P* value of <0.05. To account for variable amounts of background mRNA contamination in TRAP-seq samples, the presence of a set of cell-type-specific genes which should not be expressed in astrocytes were quantified. For each cell-type-specific gene, its expression in FPKM (fragments per kilobase per million mapped reads) in each sample was divided by its maximum FPKM in any sample, giving for each gene a per-sample measure of background contamination (with a value between 0 and 1). Per-gene contamination

values for the six genes correlated well across samples. An average was taken over the six genes to give a per-sample contamination measure (C) with a value between 0 and 1. For every other gene, the correlation of its gene expression with C over all samples was calculated, giving a per-gene measure (R) of the likelihood of a gene's apparent presence in the data as being due to background mRNA contamination. To determine how likely it was to get high values of R by chance, a test gene expression dataset containing the FPKM values from our data was created with the values scrambled between samples for each gene (in which case, this test gene expression should not be correlated with C). From this test data, the R value for each scrambled gene was created, deriving a null distribution of R values. In the real dataset, a Z-score for each gene indicating how far its own R value was from the mean of this null distribution in units of standard deviations of the null distribution was calculated. Any gene with a Z-score greater than 2 was excluded from analyses. Pathway analysis was performed using ingenuity pathway analysis (IPA) software (QIAGEN). Genes were inputted with their FPKM (cut off >5 FPKM) and corresponding log₂FC in lesions versus control. Top canonical pathways were considered significant at *P* values <0.05. Gene ontology (GO) and pathway networks were analysed using the plugin ClueGO v.2.5.4 for Cytoscape v.3.7.1 software, with the top 200 significantly upregulated genes at each time point versus control used for analysis. Statistical significance was analysed by the two-sided hypergeometric test and Bonferroni step-down correction, and grouping was based on the highest significance and GO-term fusion.

Proteomics sample preparation, mass spectrometry and analysis

Frozen corpus callosa were pulverised using the Precellys Bioruptor and bead-based lysis kit (VWR). Tissue was transferred to 1.5 ml Precellys beaded tubes with 300 µl of lysis buffer (5% SDS, 10 mM TCEP, 50 mM TEAB) before being loaded into Precellys Bioruptor for a 3 min cycle at 5500 rpm at 4 °C. Lysed tissue was transferred to 1.5 ml lo-bind Eppendorf and boiled at 95 °C for 5 min before DNA digestion with Benzonase at 37 °C for 15 min. Samples were alkylated with 20 mM iodoacetamide for 1 h at 22 °C. Protein concentration was determined using an EZQ protein quantitation kit (Invitrogen) as per the manufacturer's instructions. Protein isolation and clean up was performed using S-TRAP™ (Protifi) columns before digestion with trypsin at 1:20 enzyme:protein ratio for 2 h at 47 °C. Digested peptides were eluted from S-TRAP™ columns using 50 mM ammonium bicarbonate, followed by 0.2% aqueous formic acid and 50% aqueous acetonitrile containing 0.2% formic acid. Eluted peptides were dried down overnight before re-suspension in 5% formic acid, ready for injection onto the Orbitrap Exploris (Thermo Fisher) mass spectrometer using data-independent acquisition (DIA). Peptides (2 µg/sample) were injected onto a nanoscale C18 reverse-phase chromatography system (UltiMate 3000 RSLC nano, Thermo Scientific) and electrosprayed into an Orbitrap Exploris Mass Spectrometer (Thermo Fisher). For liquid chromatography, the following buffers were used: buffer A (0.1% formic acid in Milli-Q water (v/v)) and buffer B (80% acetonitrile and 0.1% formic acid in Milli-Q water (v/v)). Samples were loaded at 10 µl/min onto a trap column (100 µm × 2 cm, PepMap nanoViper C18 column, 5 µm, 100 Å, Thermo Scientific) equilibrated in 0.1% trifluoroacetic acid (TFA). The trap column was washed for 3 min at the same flow rate with 0.1% TFA and then switched in-line with a Thermo Scientific resolving C18 column (75 µm × 50 cm, PepMap RSLC C18 column, 2 µm, 100 Å). Peptides were eluted from the column at a constant flow rate of 300 nl/min with a linear gradient from 3% buffer B to 6% buffer B in 5 min, then from 6% buffer B to 35% buffer B in 115 min, and finally to 80% buffer B within 7 min. The column was then washed with 80% buffer B for 4 min and re-equilibrated in 3% buffer B for 15 min. Two blanks were run between each sample to reduce carry-over. The column was kept at a constant temperature of 50 °C. The data was acquired using an easy

spray source operated in positive mode with spray voltage at 2.445 kV, and the ion transfer tube temperature at 250 °C. The MS was operated in DIA mode. A scan cycle comprised a full MS scan (*m/z* range from 350–1650), with RF lens at 40%, AGC target set to custom, normalised AGC target at 300, maximum injection time mode set to custom, maximum injection time at 20 ms, microscan set to 1, and source fragmentation disabled. MS survey scan was followed by MS/MS DIA scan events using the following parameters: multiplex ions set to false, collision energy mode set to stepped, collision energy type set to normalised, HCD collision energies set to 25.5, 27 and 30%, orbitrap resolution 30,000, first mass 200, RF lens 40%, AGC target set to custom, normalised AGC target 3000%, microscan set to 1, maximum injection time 55 ms. Data for both MS Scan and MS/MS DIA Scan events were acquired in profile mode. Raw mass spectrometry data were processed using Spectronaut (Biognosys) version 14.10.201222.47784 with the DirectDIA option. The following parameters were selected: cleavage rules were set to Trypsin/P, maximum peptide length 52 amino acids, minimum peptide length 7 amino acids, maximum missed cleavages 2 and calibration mode automatic. Carbamidomethylation of cysteine was set as a fixed modification while the following variable modifications were selected: oxidation of methionine, deamidation of asparagine and glutamine and acetylation of the protein N-terminus. The FDR threshold for both precursor and protein was set at 1%. Profiling was disabled. DirectDIA data were searched against a mouse database from Uniprot release 2020 06. This database consisted of all manually annotated mouse SwissProt entries along with mouse TrEMBL entries with protein-level evidence and a manually annotated homologue within the human SwissProt database. Fold changes in protein abundance were calculated using normalised protein intensities. Normalisation was performed by dividing the intensity for each protein by the summed protein intensity for all proteins identified within an individual sample. We present examples of cholesterol pathway-associated proteins which were within the top 3000 proteins upregulated in lesions at 7 DPI.

Primary neural cell cultures

Mixed glial cultures were derived from the cortices of P0-P3 Sprague-Dawley rats of both sexes following terminal anaesthesia with pentobarbital. Microglia were isolated by collecting the floating fraction of 10-day-old mixed glial cultures following 1 h on a rotary shaker at 250 rpm at 37 °C, and plated on poly-D-lysine-coated 16-well glass chamber slides (Lab-TEK) at 5×10^4 cells per well in Dulbecco's Modified Essential Media (DMEM) with glucose (4.5 g/L), L-glutamine, pyruvate, 10% fetal calf serum and 1% penicillin/streptomycin. Microglia were either left untreated or treated with IFN γ (20 ng/ml) and LPS (0127:B8, 100 ng/ml) overnight, and Luteolin or vehicle control. Oligodendrocyte progenitor cells (OPCs) were isolated from mixed glial cultures following overnight agitation following microglia depletion as above, with astrocyte depletion in the floating fraction achieved by differential adhesion. OPCs were plated at 2×10^4 cells per well in PDL-coated plastic chamber slides (Lab-TEK) in DMEM containing glucose (4.5 g/L), L-glutamine, pyruvate, SATO (16 µg/ml putrescine, 400 ng/ml L-thyroxine, 400 ng/ml tri-iodothyroxine, 60 ng/ml progesterone, 5 ng/ml sodium selenite, 100 µg/ml bovine serum albumin fraction V, 10 µg/ml insulin, 5.5 µg/ml halo-transferrin (all from Sigma-Aldrich)), 0.5% fetal calf serum (GIBCO), 1% penicillin/streptomycin. For 2 days, cells were exposed to 10 ng/ml platelet-derived growth factor and 10 ng/ml fibroblast growth factor-2. OPCs were matured to oligodendrocytes by the withdrawal of growth factors from media for 5 days. Cells were treated with Luteolin (Tocris) or vehicle control (DMSO) for 2 days.

Astrocytes were detached from flasks following microglia and OPC depletion with 0.25% Trypsin-EDTA for 5–10 min at 37 °C. Following trypsin inactivation with fresh media, cells were separated by gentle pipetting and plated in 16-well glass chamber slides (Nunc) at

5×10^4 cells/well in DMEM with 10% FBS and 1% penicillin/streptomycin. One day post-plating, astrocytes were either left untreated or treated with CDDO^{TEA} (100 nM). Twenty-four hours later, CDDO^{TEA}-treated astrocytes were washed thoroughly with fresh media and a subset of experiments involved subsequent treatment with Luteolin (50 μ M) or CS-6253 (1 μ M). BODIPY-FL-C12 (2 μ M) was fed to astrocytes in all conditions for 6 h, then wells were washed thoroughly with fresh media to remove any residual compound not taken up by astrocytes; for experiments where astrocyte-conditioned media was to be applied to oligodendrocytes, serum was halved to 5%. After 18 h, astrocyte-conditioned media was collected and applied to oligodendrocytes, OPCs, or brain explants at a ratio of 1:1 with respective culture media.

Quantitative reverse transcription real-time polymerase chain reaction

Primary astrocytes were washed with PBS and then incubated for 10 min with RNA lysis buffer. RNA extraction was achieved using the Agilent Nanoprep kit according to the manufacturer's instructions. Complementary DNA (cDNA) was generated using the SuperScriptTM VILOTM cDNA synthesis kit (Invitrogen). The FastStart Universal SYBR Green Master mix (ROX; Roche) was used on a QuantStudio 5 Real-Time polymerase chain reaction (PCR) system. Primers used were as follows: *Hmgcs1* (5'-ATGGGGCTCGTCATAGTAA-3' and 5'-ACTCTCAGTGTCCCCGTTA-3'); *Fdps* (5'-GCACACTGACATCCAGGACAAC-3' and 5'-AGCCACTTTTTCTGGTCTCT-3'); *Mvk* (F: 5'-CTCAAGGACGGGGTCTCC-3' and R: 5'-GGCCCACTTGTTGATTGACT-3'); *Fdft1* (5'-TCCCTGACGTCTCACCTAC-3' and 5'-CCCCTCCGAATCTTCACTA-3'); *Nfe2l2* (5'-CAGCTCAAGGGCACAGTGC-3 and 5'-GTGGCCCAAGTCTTGCTCC-3'); *Gclc* (5'-CCAACCATCCGACCCTCTG-3' and 5'-TGTTCTGGCAGTGTAATCC-3'); *Nqo1* (5'-CCTTCCGAGTCATCTAGC-3' and 5'-AGCAAGGTCTTCTATTCTGGA-3'); *Gapdh* (F: 5'-GGGTGTGAACCACGAGAAT-3' and R: 5'-CCTTCCACAATGCCAAAGTT-3'); *Aldh1l1* (F: 5'-CTTTGACCTTGGGTGCCT-3' and R: 5'-ATCTGCTTTCCCATCCTTGT-3').

Immunocytochemistry

Cells were fixed with 4% PFA for 10 min, then washed in PBS and stored in PBS at 4 °C. Cells were blocked for 1 h and incubated with primary antibodies at 4 °C overnight, washed in PBS, and then incubated with secondary antibodies for 1 h at room temperature prior to counterstaining with Hoechst and coverslipping with Fluoromount-G. Primary antibodies included rat anti-Nrf2 (1:500, Cell Signalling 14596 S), rabbit anti-Aldh1l1 (1:500, Abcam ab190298), rat anti-MBP (1:250, Bio-Rad antibodies MCA409S), rabbit anti-TPPP/p25 (1:1000, Abcam ab92305), mouse anti-Sox10 (1:100, Sigma-Aldrich AMAB91297), rabbit anti-IBA1 (1:500, Abcam 178846), and mouse anti-iNOS (1:500, BD Biosciences 610329). Following washes with PBS, Alexa secondary antibodies (1:500, Life Technologies) and Hoechst (Sigma-Aldrich) were applied for 1 h. For cell death detection, a TUNEL assay was performed prior to staining according to the manufacturer's instructions (Promega G3250).

Ex vivo organotypic mouse brain explants

Following terminal anaesthesia of P0-P2 CD-1 mouse pups of both sexes with pentobarbital, cerebellum and hindbrain from were sagittally sectioned (300 μ m) on a McIlwain tissue chopper and plated onto Millipore-Millicell-CM mesh inserts (Fisher Scientific) in six-well culture plates at six explants per brain per insert. Culture media consisted of 50% minimal essential media, 25% heat-inactivated horse serum, 25% Earle's balanced salt solution (all from GIBCO), glucose (6.5 mg/ml, Sigma-Aldrich), 1% penicillin-streptomycin (Life Technologies), 1% Glutamax (Life Technologies) and 1% HEPES (Invitrogen). Demyelination was induced at 14 days in vitro by application of LPC (0.5 mg/ml, Sigma-Aldrich) for 18 h, then washed off. Cultures were exposed to primary astrocyte-conditioned media (ACM) after demyelination by treatment with 1:1 explant media:ACM or explant media:astrocyte media as a control, from 2 to 5 days post-LPC application. In separate

experiments, cultures were treated with the ABCA1 antagonist PSC833 (1–10 μ M; Tocris Bioscience) or vehicle control (DMSO) from 2 to 7 days post-LPC application. Explants were fixed with 4% PFA for 10 min, washed with PBS and stored at 4 °C until staining. Explants were permeabilized and blocked for 1 h in 5% horse serum and 0.3% Triton X-100 in PBS, and primary antibodies were applied overnight at 4 °C with gentle shaking in a humid chamber, which included rat anti-MBP (1:250; AbD Serotec, MCA409S) and mouse anti-neurofilament (1:1000; EnCor, MCA-9B12). Alexa secondary antibodies (1:500, Life Technologies, as above) were applied for 2 h, then counterstained with Hoechst and mounted with Fluoromount-G (Southern Biotech). Z-stacks of explants were acquired on an Olympus Spinning Disk confocal microscope with Slidebook software 6.

Human tissue

The research carried out in this study complies with all ethical regulations. Post-mortem tissue from multiple sclerosis (MS) patients and control cases that died of non-neurological causes were obtained via a UK prospective donor scheme with full ethical approval from the UK Multiple Sclerosis Tissue Bank (MREC/02/2/39) and their use was in accord with the terms of the informed consents obtained for the post-mortem donation under ethical approval by the National Research Ethics Committee. This included consent on sharing information on sex, age, diagnosis with MS, and cause of death. Diagnosis of MS was confirmed by neuropathological means by F. Roncaroli (Imperial College London) and clinical history was provided by R. Nicholas (Imperial College London). Snap-frozen unfixed tissue blocks (2 × 2 × 1 cm³) were cut at 10 μ m and stored at –80 °C. MS lesions were classified according to the International Classification of Neurological Disease using Luxol Fast Blue (LFB) staining and CD68+ immunoreactivity. Cases included both sexes. Healthy control tissue showed intact myelin, no myelin debris, and few CD68+ cells. Fully remyelinated lesions showed the intermediate intensity of LFB, little to no myelin debris, and few CD68+ cells. Active lesions showed a diffuse LFB border with demyelination, and abundance of myelin debris throughout the lesion, and high numbers of CD68+ cells. Inactive lesions showed significant demyelination, no myelin debris, tissue destruction, and low CD68+ cell numbers. Tissue blocks from four controls and eight MS cases were analysed. Sections were fixed in 4% PFA for 1 h, washed with Tris-buffered saline (TBS) and permeabilized in methanol for 10 min at –20 °C. Following three washes in 0.001% Triton X-100 in TBS, sections were microwaved at medium power in Vector Unmasking Solution for 5 min, heated for 20 min in the oven at 60 °C and cooled down for 10 min. After three washes with 0.001% Triton X-100, sections were blocked for 5 min in Peroxide Bloxall (Vector Labs), then in blocking buffer for 1 h (10% normal horse serum, 0.5% Triton X-100 in TBS). Primary antibodies were sequentially applied overnight at 4 °C, and included rabbit anti-HMGCS1 (1:500, Invitrogen PA5-29488), rabbit anti-HMOX1 (1:100, Enzo ADI-SPA-895-D), rabbit anti-TPPP/p25 (1:100, Abcam ab92305), rabbit anti-active Caspase-3 (1:500, BD Pharmingen 559565), goat anti-NQO1 (1:100 Abcam ab2346), mouse anti-Olig2 (1:100, EMD Millipore MABN50), chicken anti-GFAP (1:100, Cambridge Bioscience 829401) and rat anti-Nrf2 (1:100, Cell Signalling 14596 S). After three washes in 0.001% Triton X-100, sections were incubated with a secondary antibody (HRP ImmPress, Vector Labs) for 1 h at room temperature. Following three washes with 0.001% Triton X-100, slides were incubated with Opal fluorophore-conjugated tyramide signal amplification (TSA; 1:100, Akoya Biosciences). After the application of tyramides, slices were microwaved at medium power in Vector Unmasking Solution for 8 min, cooled for 20 min then washed in 0.001% Triton X-100. For detection of GFAP, HMOX1 and HMGCS1, Alexa-conjugated secondary antibodies (1:500, Life Technologies) were applied for 2 h after tyramides. On the last secondary antibody application, slides were counterstained with Hoechst and coverslipped with Fluoromount-G. Entire tissue sections were imaged using a Zeiss

AxioScan Z.1 SlideScanner at a single z-plane using Zen2 software. Three regions of interest per lesion were chosen in a blinded manner, cell densities were analysed (also blinded) and averaged per sample per lesion type.

Human brain single nuclei RNA sequencing analysis

Published single nuclei RNA sequences from control and multiple sclerosis brains were downloaded from NCBI (Accession number PRJNA544731)²⁹. This was based on the sequencing of nine control cases, eight MS cases with active lesions and four MS cases with inactive lesions. Cellranger (version 3.1.0) count was used to map reads from each sample to GRCh38 using default parameters, and output from each sample was aggregated with Cellranger Aggr. The aggregated filtered feature barcode matrix was imported into Seurat (version 4.0.4) and filtered based on quality metrics. Cells with fewer than 200 or greater than 2500 RNA features were excluded, as were cells with >15% mitochondrial RNA. Features which were present in <5 cells were discarded. Read counts were normalised using Log1p transformation. Variance stabilising transformation was used to identify the top 2000 most variable features. Data were scaled to the cell count total and centred, and effects of percent mitochondrial RNA and number of UMIs was regressed out. A shared nearest neighbour graph was constructed with the top ten principal components from the scaled data to identify clusters. Astrocytes were identified based on the expression of astrocytic marker genes *AQP4* and *GFAP* visualised by the t-SNE plot. Annotated astrocytes were extracted and re-clustered using the method described above to identify sub-clusters. Non-protein coding genes were removed from cluster gene lists. Cluster gene lists were computed by finding differentially expressed genes between cluster 1 and all other cells using the Seurat function FindMarkers, setting the minimum percent of cells expressing a feature in either comparison group to 5% and the log fold change threshold to 0. For the enrichment of Nrf2-target genes, a minimum percent threshold of gene abundance was set to 5%. Mouse astrocyte transcriptomes from our dataset were compared to published single nuclei sequences from multiple sclerosis lesions using Analysis Match from OmicSoft expression analysis (Ingenuity Pathway Analysis software, QIAGEN).

Imaging processing and quantification

ImageJ (versions 1.51j to 1.53t) was used to convert maximum projection images into thresholded 8-bit RGB tiffs for astrocyte and oligodendrocyte counts, and to separate nuclei by watershed segmentation. Thresholded images were used to measure the percentage area of corpus callosum covered by MBP or CNPase staining over the total lesion area of the image. Imaris 9.0.0 software was used to quantify astrocytes positive for various markers in z-stacks using ImarisColoc and ImarisSurfaces, where thresholding was achieved using absolute intensity and the size of each 'surface' was adjusted so that each was the size of a cell. Two regions of interest were analysed and averaged per stain, repeated for three sections per animal, from which a mean per animal was obtained. For remyelination index quantification, images were cropped in five z-planes and imported into Velocity software v.6.3 (Perkin Elmer), in which the voxels for each channel (NFH and MBP) were measured as well as the co-localisation between both channels. The co-localisation value was normalised to the NFH voxel counts to account for variations in axonal density.

Statistics and reproducibility

The mouse sample size was informed by our previous work in glial cell responses in CNS remyelination, and subsequently calculated by a two-sided 95% confidence interval using the normal approximation method using OpenEpi software. For human tissue staining, we used $n=3-11$ white matter areas, due to tissue availability and in line with our previous work on neuropathology of MS lesions. Statistical analysis was performed using GraphPad Prism 7–9 software. The

Shapiro–Wilk test was used to assess Gaussian distribution, and then statistical analysis was performed (two-tailed unpaired Student's *t*-test with Welch's correction or ANOVA with Tukey's multiple comparisons test, or Kolmogorov–Smirnov test or Kruskal–Wallis test with Dunn's multiple comparisons test). When two independent variables were compared (e.g. treatment and time), a two-way ANOVA was applied with Sidak's multiple comparisons test or Bonferroni correction. Data were represented as mean \pm standard error of means (s.e.m.). *P* values <0.05 were considered statistically significant and are indicated in the figure legends. For representative micrographs in the paper, represent experiments repeated a minimum of three times with similar results.

Reporting summary

Further information on research design is available in the Nature Portfolio Reporting Summary linked to this article.

Data availability

The TRAP-sequencing data has been deposited in EMBL-EBI's ArrayExpress under the accession number: [E-MTAB-9270](https://www.ebi.ac.uk/arrayexpress/experiments/E-MTAB-9270). Paired-end reads were mapped to the primary assembly of the mouse (mm10) reference genome contained in Ensembl release 93 (http://jul2018.archive.ensembl.org/Mus_musculus/info/Index). The human single nuclei RNA sequencing data was sourced from NCBI (Accession number PRJNA544731). Proteomics data were searched against a mouse database from Uniprot release 2020 06. The mass spectrometry proteomics data have been deposited to the ProteomeXchange Consortium via the PRIDE partner repository with the dataset identifier [PXD041850](https://www.ebi.ac.uk/pride/projects/dataset/PXD041850). Source data are provided with this paper.

References

- Franklin, R. J. & Ffrench-Constant, C. Regenerating CNS myelin — from mechanisms to experimental medicines. *Nat. Rev. Neurosci.* **18**, 17 (2017).
- Heß, K. et al. Lesion stage-dependent causes for impaired remyelination in MS. *Acta Neuropathol.* **140**, 359–375 (2020).
- Lubetzki, C., Zalc, B., Williams, A., Stadelmann, C. & Stankoff, B. Remyelination in multiple sclerosis: from basic science to clinical translation. *Lancet Neurol.* **19**, 678–688 (2020).
- Włodarczyk, A. et al. A novel microglial subset plays a key role in myelinogenesis in developing brain. *EMBO J.* **36**, 3292–3308 (2017).
- Hagemeyer, N. et al. Microglia contribute to normal myelinogenesis and to oligodendrocyte progenitor maintenance during adulthood. *Acta Neuropathol.* **134**, 441–458 (2017).
- Miron, V. E. et al. M2 microglia and macrophages drive oligodendrocyte differentiation during CNS remyelination. *Nat. Neurosci.* **16**, 1211–1218 (2013).
- Gibson, E. M. et al. Methotrexate chemotherapy induces persistent tri-glia dysregulation that underlies chemotherapy-related cognitive impairment. *Cell* **176**, 43–55 e13 (2019).
- Lloyd, A. F. et al. Central nervous system regeneration is driven by microglial necroptosis and repopulation. *Nat. Neurosci.* **22**, 1046–1052 (2019).
- Dutta, D. J. et al. Regulation of myelin structure and conduction velocity by perinodal astrocytes. *Proc. Natl Acad. Sci. USA* **115**, 11832–11837 (2018).
- Camargo, N. et al. Oligodendroglial myelination requires astrocyte-derived lipids. *PLoS Biol.* **15**, e1002605 (2017).
- Molina-Gonzalez, I. & Miron, V. E. Astrocytes in myelination and remyelination. *Neurosci. Lett.* **713**, 134532 (2019).
- Skripuletz, T. et al. Astrocytes regulate myelin clearance through recruitment of microglia during cuprizone-induced demyelination. *Brain* **136**, 147–167 (2013).
- Franklin, R. J., Crang, A. J. & Blakemore, W. F. Transplanted type-1 astrocytes facilitate repair of demyelinating lesions by host

- oligodendrocytes in adult rat spinal cord. *J. Neurocytol.* **20**, 420–430 (1991).
14. Blakemore, W. F., Gilson, J. M. & Crang, A. J. The presence of astrocytes in areas of demyelination influences remyelination following transplantation of oligodendrocyte progenitors. *Exp. Neurol.* **184**, 955–963 (2003).
 15. Boyd, A., Zhang, H. & Williams, A. Insufficient OPC migration into demyelinated lesions is a cause of poor remyelination in MS and mouse models. *Acta Neuropathol.* **125**, 841–859 (2013).
 16. Dombrowski, Y. et al. Regulatory T cells promote myelin regeneration in the central nervous system. *Nat. Neurosci.* **20**, 674–680 (2017).
 17. Heiman, M., Kulicke, R., Fenster, R. J., Greengard, P. & Heintz, N. Cell type-specific mRNA purification by translating ribosome affinity purification (TRAP). *Nat. Protoc.* **9**, 1282–1291 (2014).
 18. Zamanian, J. L. et al. Genomic analysis of reactive astrogliosis. *J. Neurosci.* **32**, 6391–6410 (2012).
 19. Wheeler, M. A. et al. MAFG-driven astrocytes promote CNS inflammation. *Nature* **578**, 593–599 (2020).
 20. Decker, L. & French-Constant, C. Lipid rafts and integrin activation regulate oligodendrocyte survival. *J. Neurosci.* **24**, 3816–3825 (2004).
 21. Itoh, N. et al. Cell-specific and region-specific transcriptomics in the multiple sclerosis model: Focus on astrocytes. *Proc. Natl Acad. Sci. USA* **115**, E302–E309 (2018).
 22. Boisvert, M. M., Erikson, G. A., Shokhiev, M. N. & Allen, N. J. The aging astrocyte transcriptome from multiple regions of the mouse brain. *Cell Rep.* **22**, 269–285 (2018).
 23. Chartoumpakis, D. V. & Kensler, T. W. New player on an old field; the Keap1/Nrf2 pathway as a target for treatment of type 2 diabetes and metabolic syndrome. *Curr. Diabetes Rev.* **9**, 137–145 (2013).
 24. Kitteringham, N. R. et al. Proteomic analysis of Nrf2 deficient transgenic mice reveals cellular defence and lipid metabolism as primary Nrf2-dependent pathways in the liver. *J. Proteom.* **73**, 1612–1631 (2010).
 25. Tanaka, Y. et al. NF-E2-related factor 2 inhibits lipid accumulation and oxidative stress in mice fed a high-fat diet. *J. Pharm. Exp. Ther.* **325**, 655–664 (2008).
 26. Zhang, Y. K., Yeager, R. L., Tanaka, Y. & Klaassen, C. D. Enhanced expression of Nrf2 in mice attenuates the fatty liver produced by a methionine- and choline-deficient diet. *Toxicol. Appl. Pharm.* **245**, 326–334 (2010).
 27. Vargas, M. R., Johnson, D. A., Sirkis, D. W., Messing, A. & Johnson, J. A. Nrf2 activation in astrocytes protects against neurodegeneration in mouse models of familial amyotrophic lateral sclerosis. *J. Neurosci.* **28**, 13574–13581 (2008).
 28. Sigfridsson, E. et al. Astrocyte-specific overexpression of Nrf2 protects against optic tract damage and behavioural alterations in a mouse model of cerebral hypoperfusion. *Sci. Rep.* **8**, 12552 (2018).
 29. Schirmer, L. et al. Neuronal vulnerability and multilineage diversity in multiple sclerosis. *Nature* **573**, 75–82 (2019).
 30. Hafiane, A., Bielicki, J. K., Johansson, J. O. & Genest, J. Novel apo E-derived ABCA1 agonist peptide (CS-6253) promotes reverse cholesterol transport and induces formation of pre-beta-1 HDL in vitro. *PLoS ONE* **10**, e0131997 (2015).
 31. Ortinski, P. I. et al. Selective induction of astrocytic gliosis generates deficits in neuronal inhibition. *Nat. Neurosci.* **13**, 584–591 (2010).
 32. Papouin, T., Dunphy, J. M., Tolman, M., Dineley, K. T. & Haydon, P. G. Septal cholinergic neuromodulation tunes the astrocyte-dependent gating of hippocampal NMDA receptors to wakefulness. *Neuron* **94**, 840–854 e847 (2017).
 33. Wu, Z. et al. Gene therapy conversion of striatal astrocytes into GABAergic neurons in mouse models of Huntington's disease. *Nat. Commun.* **11**, 1105 (2020).
 34. Gupta, K. et al. Human embryonic stem cell derived astrocytes mediate non-cell-autonomous neuroprotection through endogenous and drug-induced mechanisms. *Cell Death Differ.* **19**, 779–787 (2012).
 35. Liby, K. et al. The synthetic triterpenoids, CDDO and CDDO-imidazole, are potent inducers of heme oxygenase-1 and Nrf2/ARE signaling. *Cancer Res.* **65**, 4789–4798 (2005).
 36. Huppke, P. et al. Activating de novo mutations in NFE2L2 encoding NRF2 cause a multisystem disorder. *Nat. Commun.* **8**, 818 (2017).
 37. Ioannou, M. S. et al. Neuron-astrocyte metabolic coupling protects against activity-induced fatty acid toxicity. *Cell* **177**, 1522–1535 e1514 (2019).
 38. van Horsen, J. et al. Nrf2 and DJ1 are consistently upregulated in inflammatory multiple sclerosis lesions. *Free Radic. Biol. Med.* **49**, 1283–1289 (2010).
 39. Licht-Mayer, S. et al. Cell type-specific Nrf2 expression in multiple sclerosis lesions. *Acta Neuropathol.* **130**, 263–277 (2015).
 40. Taliou, A., Zintzaras, E., Lykouras, L. & Francis, K. An open-label pilot study of a formulation containing the anti-inflammatory flavonoid luteolin and its effects on behavior in children with autism spectrum disorders. *Clin. Ther.* **35**, 592–602 (2013).
 41. Tang, X. et al. Luteolin inhibits Nrf2 leading to negative regulation of the Nrf2/ARE pathway and sensitization of human lung carcinoma A549 cells to therapeutic drugs. *Free Radic. Biol. Med.* **50**, 1599–1609 (2011).
 42. Imran, M. et al. Luteolin, a flavonoid, as an anticancer agent: a review. *Biomed. Pharmacother.* **112**, 108612 (2019).
 43. Johnson, D. A., Amirahmadi, S., Ward, C., Fabry, Z. & Johnson, J. A. The absence of the pro-antioxidant transcription factor Nrf2 exacerbates experimental autoimmune encephalomyelitis. *Toxicol. Sci.* **114**, 237–246 (2010).
 44. Draheim, T. et al. Activation of the astrocytic Nrf2/ARE system ameliorates the formation of demyelinating lesions in a multiple sclerosis animal model. *Glia* **64**, 2219–2230 (2016).
 45. Saher, G. et al. High cholesterol level is essential for myelin membrane growth. *Nat. Neurosci.* **8**, 468–475 (2005).
 46. Saher, G. & Stumpf, S. K. Cholesterol in myelin biogenesis and hypomyelinating disorders. *Biochim. Biophys. Acta* **1851**, 1083–1094 (2015).
 47. Hubler, Z. et al. Accumulation of 8,9-unsaturated sterols drives oligodendrocyte formation and remyelination. *Nature* **560**, 372–376 (2018).
 48. Voskuhl, R. R. et al. Gene expression in oligodendrocytes during remyelination reveals cholesterol homeostasis as a therapeutic target in multiple sclerosis. *Proc. Natl Acad. Sci. USA* **116**, 10130–10139 (2019).
 49. Berghoff, S. A. et al. Microglia facilitate repair of demyelinated lesions via post-squalene sterol synthesis. *Nat. Neurosci.* **24**, 47–60 (2021).
 50. Miron, V. E. et al. Statin therapy inhibits remyelination in the central nervous system. *Am. J. Pathol.* **174**, 1880–1890 (2009).
 51. Theoharides, T. C., Asadi, S. & Panagiotidou, S. A case series of a luteolin formulation (NeuroProtek®) in children with autism spectrum disorders. *Int. J. Immunopathol. Pharm.* **25**, 317–323 (2012).
 52. Theoharides, T. C., Stewart, J. M., Hatziagelaki, E. & Kolaitis, G. Brain “fog,” inflammation and obesity: key aspects of neuropsychiatric disorders improved by luteolin. *Front. Neurosci.* **9**, 225 (2015).
 53. Tsilioni, I., Taliou, A., Francis, K. & Theoharides, T. C. Children with autism spectrum disorders, who improved with a luteolin-containing dietary formulation, show reduced serum levels of TNF and IL-6. *Transl. Psychiatry* **5**, e647–e647 (2015).
 54. Voskuhl, R. R. et al. Estriol combined with glatiramer acetate for women with relapsing-remitting multiple sclerosis: a randomised, placebo-controlled, phase 2 trial. *Lancet Neurol.* **15**, 35–46 (2016).

55. MacKenzie-Graham, A. et al. Estriol-mediated neuroprotection in multiple sclerosis localized by voxel-based morphometry. *Brain Behav.* **8**, e01086 (2018).
56. Mei, F. et al. Micropillar arrays as a high-throughput screening platform for therapeutics in multiple sclerosis. *Nat. Med.* **20**, 954–960 (2014).
57. Lloyd, A. F. & Miron, V. E. The pro-remyelination properties of microglia in the central nervous system. *Nat. Rev. Neurol.* **15**, 447–458 (2019).
58. De La Fuente, A. G. et al. Pericytes stimulate oligodendrocyte progenitor cell differentiation during CNS remyelination. *Cell Rep.* **20**, 1755–1764 (2017).
59. Boehm-Cagan, A. et al. ABCA1 agonist reverses the apoE4-driven cognitive and brain pathologies. *J. Alzheimers Dis.* **54**, 1219–1233 (2016).

Acknowledgements

This work was funded by a studentship from the United Kingdom Multiple Sclerosis Society (to V.E.M.; grant no. 54), a Medical Research Council and United Kingdom Multiple Sclerosis Society Career Development Award (to V.E.M.; grant no. MR/M020827/1), a Medical Research Council Senior Non-Clinical Fellowship (to V.E.M.; grant no. MRC/V031260/1), funds from the Medical Research Council Centre for Reproductive Health (grant no. MR/N02256/1), and the John David Eaton Chair in Multiple Sclerosis Research from St. Michael's Hospital Foundation. The cuprizone studies were supported by the German Research Foundation (T.K.; grant no. SFB-TR128-B7) and the Hannover Medical School (Hochschulinterne Leistungsförderung; M.S.). We thank the United Kingdom Multiple Sclerosis Society Tissue Bank for providing tissue. We thank A. Rooney, N. McNamara, L. Ryan, L. Zoupi, S. Jaekel and M. Blesa for helpful discussions and F. Roncaroli, R. Nicholas and C. Watkins for technical support. Diagrams were created using BioRender.com.

Author contributions

I.M.-G. co-designed the study, carried out the experiments, analysed and interpreted the data, co-made the figures and co-wrote the manuscript. Z.J. assisted in TRAP protocols and provided RNA sequencing data for non-lesioned GFAP-Nrf2 mouse astrocytes. O.D. and K.E. performed TRAP-RNA sequencing and snRNA sequencing analyses. R.K.H., L.H.F., S.A.K. and A.M. assisted with surgical procedures, tissue processing and cryosectioning, cultures and immunostaining. A.F.L. and A.J.M.H. performed proteomics analysis. V.G., T.S. and M.S. carried out astrocyte depletion experiments. J.A.J. made GFAP-Nrf2 mice. J.A.F. and J.H.F. assisted in the breeding and

genotyping of transgenic mice. T.K. performed cuprizone model experiments. A.W. provided human tissue pathological mapping. S.C. and G.E.H. co-supervised the project and contributed to experimental design, interpretation and manuscript editing. V.E.M. supervised the project, guided experimental design and interpretation, co-made the figures and co-wrote the manuscript.

Competing interests

The authors declare no competing interests.

Additional information

Supplementary information The online version contains supplementary material available at <https://doi.org/10.1038/s41467-023-39046-8>.

Correspondence and requests for materials should be addressed to Veronique E. Miron.

Peer review information *Nature Communications* thanks Mikael Simons, and the other, anonymous, reviewer(s) for their contribution to the peer review of this work. A peer review file is available.

Reprints and permissions information is available at <http://www.nature.com/reprints>

Publisher's note Springer Nature remains neutral with regard to jurisdictional claims in published maps and institutional affiliations.

Open Access This article is licensed under a Creative Commons Attribution 4.0 International License, which permits use, sharing, adaptation, distribution and reproduction in any medium or format, as long as you give appropriate credit to the original author(s) and the source, provide a link to the Creative Commons license, and indicate if changes were made. The images or other third party material in this article are included in the article's Creative Commons license, unless indicated otherwise in a credit line to the material. If material is not included in the article's Creative Commons license and your intended use is not permitted by statutory regulation or exceeds the permitted use, you will need to obtain permission directly from the copyright holder. To view a copy of this license, visit <http://creativecommons.org/licenses/by/4.0/>.

© The Author(s) 2023

¹United Kingdom Dementia Research Institute at The University of Edinburgh, Edinburgh Medical School, Edinburgh EH16 4TJ, UK. ²United Kingdom Multiple Sclerosis Society Edinburgh Centre for Multiple Sclerosis Research, University of Edinburgh, Edinburgh EH16 4TJ, UK. ³Center for Discovery Brain Sciences, University of Edinburgh, Edinburgh EH16 4SB, UK. ⁴Medical Research Council Centre for Reproductive Health, University of Edinburgh, Edinburgh EH16 4TJ, UK. ⁵Wellcome Trust Translational Neuroscience PhD programme, Edinburgh, UK. ⁶Cell Signalling and Immunology, School of Life Sciences, University of Dundee, Dundee DD1 5EH, UK. ⁷Department of Clinical Neuroimmunology and Neurochemistry, Department of Neurology, Medizinische Hochschule Hannover, Hannover 30625, Germany. ⁸Division of Pharmaceutical Sciences, University of Wisconsin, Madison, WI 53705, USA. ⁹Molecular and Environmental Toxicology Centre, University of Wisconsin, Madison, WI 53706, USA. ¹⁰Center for Neuroscience, University of Wisconsin, Madison, WI 53705, USA. ¹¹Waisman Centre, University of Wisconsin, Madison, WI 53705, USA. ¹²Institute of Neuropathology, University Hospital Muenster, Muenster D-48129, Germany. ¹³Centre for Regenerative Medicine, Institute for Regeneration and Repair, University of Edinburgh, Edinburgh EH16 5UU, UK. ¹⁴Centre for Clinical Brain Sciences, University of Edinburgh, Edinburgh EH16 4SB, UK. ¹⁵BARLO Multiple Sclerosis Centre, St. Michael's Hospital, Toronto, ON M5B 1W8, Canada. ¹⁶Keenan Centre for Biomedical Research at St. Michael's Hospital, Toronto, ON M5B 1T8, Canada. ¹⁷Department of Immunology, University of Toronto, Toronto, ON M5S 1A8, Canada. ✉ e-mail: veronique.miron@unityhealth.to